Preprint
UCRL-JC-151176

High-Resolution, Numerical Modeling of Energetic and Inert Materials at Large Deformation Rates

J.J. Yoh, D.S. Stewart

This article was submitted to Combustion Theory and Modeling

U.S. Department of Energy

Lawrence
Livermore
National
Laboratory

November 27, 2002

Approved for public release; further dissemination unlimited

High-resolution, numerical modeling of energetic and inert materials at large deformation rates

Jack J. Yoh‡ and D. Scott Stewart§

Abstract.

This paper describes the methodology used to build a high-resolution, multi-material hydrocode that is formulated to be third order in time and fourth order in space. The hydrocode is suitable for simulating high-speed impact and interaction of energetic and inert materials. Energetic materials are modeled by the reactive Euler equations. The inert materials can be modeled by either the Euler equations or by constitutive laws that can describe metals. Level set functions are used to track the motion of multi-material interfaces between fluids, solids and free surfaces (or voids). A technique is used to extrapolate material states into extended ghost node regions to enforce boundary conditions. A standard pressure update is used near the material/material interfaces. The algorithms are verified with a collection of standard test problems, and the function of the code is demonstrated with a series of representative applications that include: copper rod impact, explosive rate-stick, explosive welding, and the impact of a copper plate by a cylindrical detonation.

‡ Lawrence Livermore National Laboratory, Livermore, CA 94551, USA
§ Theoretical and Applied Mechanics, University of Illinois, Urbana, IL 61801, USA.
To whom correspondence should be addressed (yoh1@llnl.gov)

1. Introduction

High-speed impact of materials generates strong shock waves, large rates of deformations and generates hydrodynamic pressures that are often much greater than the deviatoric stresses. Then, variants of the standard Euler equations for compressible flow can be used to model materials with deviatoric strength. The dominant physical mechanisms satisfy the Euler equations to a first approximation, and the effects associated with deviatoric strength are in some sense a small correction. We describe the numerical methodology that we used to construct a high resolution (in both space and time) code that can be used to simulate multi-material interactions at high strain rates and detonation in explosives. Our purpose is to offer enough detail so that interested readers can reproduce this capability with a minimum of effort and use the resulting code to good effect. One of our target applications for this code is explosively driven material processing.

In the past, hydrodynamic codes have been developed to model multi-dimensional, multi-material interactions with high-rate of deformations in the presence of strong shock waves [1, 2, 3]. In particular, CTH is a 3-D hydrocode developed at Sandia National Laboratories [1, 4], and it has been successfully applied to a large variety of strong shock problems, which include hypervelocity impact and effects of detonating high explosives. Both analytic and tabular equations of state (EOS) for solid, liquid, vapor, gas–liquid mixed phase and solid–liquid mixed phase have been implemented [4]. Similar hydrocodes, MESA (a precursor) [3] and PAGOSA [2], both developed at Los Alamos National Laboratory, are based on finite difference approximations on an Eulerian mesh. Such codes are representative of a certain class of hydrocodes. These codes typically solve the conservation of mass, momentum, and energy equations across the ‘fixed’ interface in two steps: A

Lagrangian step where the cell distorts and follows the material motion, followed by a rezone step where the distorted cells are mapped back to the Eulerian mesh.

Typically these hydrocodes are first order in time and second order in space. Our high-resolution approach uses fourth-order convex ENO for the spatial discretization and third-order TVD Runge–Kutta for time advancement. Our treatment of material interfaces uses level sets and is fairly simple and robust. Enforcement of jump conditions across the material interface is achieved by applying a ghost-node-populating technique to interpolate data into extended regions. The time advancement is based on the method of lines, and it enables multi-dimensional calculations without time splitting and allows efficient implementation of Runge–Kutta schemes at orders higher than two.

The physical models we use include an ideal equation of state (EOS) for an inert compressible gas, an ideal EOS reactive flow model for a high-explosive (HE) that uses the reaction rate law found in [5], a Mie–Gruneisen EOS for inert solid, Blatz–Ko elasticity model for an elastic, rubbery solid, [6], an elasto–plastic model for metal with isotropic linear hardening and Johnson–Cook hardening laws.

We carry out validation exercises in one and two dimensions to test our models and the high-resolution numerics with level set interface tracking. First, we consider standard shock tube tests with two different gases, and we demonstrate the spatial rate of convergence of the high-order scheme. To test the reactive Euler flow solver, we reproduce the one-dimensional ZND detonation wave structure for the ABS model described in Ref. [5]. The third numerical validation is a benchmark simulation of Taylor copper-rod impact test, and we compare against a similar simulation that used an adaptive finite-element method described in [7]. A fourth exercise computes detonation propagating in an explosive rate-stick experiment. The rate-stick is a cylindrical tube or finite-width slab of explosive confined by inert material. The stick is initiated at one end by a high pressure/temperature region, and a curved detonation wave emerges and eventually propagates steadily down the axis of the stick. The steady detonation speed and the angle of inert shock transmitted to the adjacent material at the interface are compared against a similar benchmark computation by Aslam [8] that was carried out with an advanced adaptive mesh refinement code.

Following these validations, we demonstrate capabilities of our multi-dimensional hydrocode by applying it to problems that reflect our current research interests in explosively driven materials processing. First, we simulate a rate-stick experiment involving HE, copper, and void layers, and we observe how the copper layer is deformed. Then, we simulate explosive welding of copper and high-strength steel plates that are initially unbound. Upon detonating an explosive in outer layer, the two metals come in contact in both shear and impact motions that cause an instability at the material interface. A final application of the model is the two-dimensional metal-plate-impact experiment. A plate of thickness 5 mm is shocked by a spherically propagating detonation wave. Intermediate and final deformations of the metal plate are of interest while the plastic strain distribution upon contact with the detonation wave serves to characterize the damage to the plate.

2. A high-order hyperbolic solver

The general conservation laws of multi-dimensional, multi-material physics can be written as

$$\frac{\partial \boldsymbol{U}}{\partial t} + \frac{\partial \boldsymbol{F}}{\partial x} + \frac{\partial \boldsymbol{G}}{\partial y} = \boldsymbol{S}(\boldsymbol{U}) \tag{1}$$

where the variables represent a vector of conserved variables $\boldsymbol{U}$, spatial fluxes in x and y-directions $\boldsymbol{F}$ and $\boldsymbol{G}$, and a source, $\boldsymbol{S}$.

The discretized system of PDEs in (1) can be solved by independent steps of space and time integration. For our two-dimensional system, the x and y fluxes are treated with the fourth-order convex ENO scheme, [9]. Once the two advection terms are approximated by spatial differences, equation (1) is approximated by a system of ODEs (rather than PDEs) that are solved in time with a third-order TVD Runge-Kutta scheme that is guaranteed to be total-variation diminishing in the sense of [10].

2.1. Discretizations in time

The third-order TVD Runge-Kutta algorithm for time advance in this work is given by

$$\begin{aligned}
\boldsymbol{U}_1 &= \boldsymbol{U}_0 + \Delta t[\boldsymbol{L}(\boldsymbol{U}_0) + \boldsymbol{S}(\boldsymbol{U}_0)]\,,\\
\boldsymbol{U}_2 &= \boldsymbol{U}_0 + \frac{1}{4}\Delta t[\boldsymbol{L}(\boldsymbol{U}_0) + \boldsymbol{S}(\boldsymbol{U}_0)] + \frac{1}{4}\Delta t[\boldsymbol{L}(\boldsymbol{U}_1) + \boldsymbol{S}(\boldsymbol{U}_1)]\,,\\
\boldsymbol{U}_3 &= \boldsymbol{U}_0 + \frac{1}{6}\Delta t[\boldsymbol{L}(\boldsymbol{U}_0) + \boldsymbol{S}(\boldsymbol{U}_0)]\\
&\quad + \frac{1}{6}\Delta t[\boldsymbol{L}(\boldsymbol{U}_1) + \boldsymbol{S}(\boldsymbol{U}_1)] + \frac{2}{3}\Delta t[\boldsymbol{L}(\boldsymbol{U}_2) + \boldsymbol{S}(\boldsymbol{U}_2)]\,,
\end{aligned} \tag{2}$$

where $\boldsymbol{L}$ and $\boldsymbol{S}$ now represent discretized spatial derivatives in x (and y if 2-D) direction, and the source terms of (1), respectively. The high-order spatial approximation to the derivative fluxes represented by $\boldsymbol{L}$ will be discussed next.

2.2. General ENO scheme for spatial discretization

The conservative form of a one-dimensional hyperbolic PDE is given by

$$\frac{\partial u}{\partial t} + \frac{\partial f(u)}{\partial x} = 0. \tag{3}$$

The time derivative is maintained but the spatial derivative is replaced by spatial discretization. The resulting ODE is a semi-discretized equation,

$$\frac{du}{dt} + \frac{1}{\Delta x}(\hat{f}_{j+\frac{1}{2}} - \hat{f}_{j-\frac{1}{2}}) = 0. \tag{4}$$

The numerical fluxes are the ingredient that determine the spatial order of accuracy, and different versions of ENO (or earlier versions of TVD) schemes give recipes for the construction of fluxes [10, 9]. Next, we describe the recipe that leads to the high-order convex ENO approximation.

The fluxes in (4) are generated from the combination of the upwind and downwind portions represented by

$$f^{+}_{j+\frac{1}{2}}(u) = \frac{1}{2}(f(u) + \alpha_{j+\frac{1}{2}}u), \quad f^{-}_{j+\frac{1}{2}}(u) = \frac{1}{2}(f(u) - \alpha_{j+\frac{1}{2}}u). \tag{5}$$

We note variation in the definition of α controls the amount of viscosity or diffusion of a scheme and results in different versions of these fluxes. In this work, the local Lax–Friedrichs fluxes are employed by specifying

$$\alpha_{j+\frac{1}{2}} = \max_{\min(u_j,u_{j+1}) \le u \le \max(u_j,u_{j+1})} \left| \frac{df}{du} \right|, \tag{6}$$

where $\alpha_{j+\frac{1}{2}}$ is the largest eigenvalue of the flux Jacobian, df/du, evaluated on the local computational domain of (u_j, u_{j+1}). The first-order local Lax–Friedrichs flux is defined as follows:

$$\hat{f}_{j+\frac{1}{2}} = f^{+}_{j+\frac{1}{2}}(u_j) + f^{-}_{j+\frac{1}{2}}(u_{j+1}). \tag{7}$$

The second-order flux is written as

$$\begin{aligned}\hat{f}_{j+\frac{1}{2}} &= \frac{1}{2}[f(u_{j+1}) + f(u_j) - \alpha_{j+\frac{1}{2}}(u_{j+1} - u_j)] \\ &+\frac{1}{4}[\ell(r_j^+)(\Delta_+ f(u_j) + \alpha_{j+\frac{1}{2}}\Delta_+ u_j) - \ell(r_{j+1}^-)(\Delta_+ f(u_{j+1}) - \alpha_{j+\frac{1}{2}}\Delta_+ u_{j+1})]\end{aligned} \tag{8}$$

where $\Delta_\pm u_j$, r_j^+, and r_{j+1}^- are given by

$$\Delta_\pm u_j = \pm(u_{j\pm 1} - u_j), \tag{9}$$

$$r_j^+ = \frac{(\Delta_- f(u_j) + \alpha_{j+\frac{1}{2}}\Delta_- u_j)}{(\Delta_+ f(u_j) + \alpha_{j+\frac{1}{2}}\Delta_+ u_j)}, \quad r_{j+1}^- = \frac{(\Delta_- f(u_{j+1}) - \alpha_{j+\frac{1}{2}}\Delta_- u_{j+1})}{(\Delta_+ f(u_{j+1}) - \alpha_{j+\frac{1}{2}}\Delta_+ u_{j+1})}. \tag{10}$$

For ℓ, we chose the minmod limiter, given by

$$\ell(r) = \max\left(0, \min(r, 1)\right). \tag{11}$$

2.2.1. High-order convex ENO scheme The first and second-order convex ENO fluxes are the local Lax–Friedrichs fluxes that use the minmod limiter as defined in the previous section. Next, we build the high-order convex ENO fluxes. To do this we define a function $H(x)$, whose derivative with respect to x_j represents a non-oscillatory approximation to the flux $\hat{f}(x)$ at each grid points. In other words, $\left(H^{(n)+}(x_j)\right)' = f^{(n)+}_{j+\frac{1}{2}}(u_j)$ for the upwind component of the n-th order convex ENO flux. A detailed example of the ENO construction is discussed in the Appendix.

The upwinding interpolant involving the points (x_{j-1}, x_j) and the first-order polynomial interpolant to the upwind flux is

$$H^{(1)+}(x) = H[x_{j-1}, 0] + H[x_j, 1](x - x_{j-1}), \tag{12}$$

where the square bracket denotes the divided difference coefficient of the Newton interpolating polynomial [11]. The second argument in the square bracket denotes the order of these coefficients. A table of these coefficients for each points in the computing grids can be constructed in a straight forward manner, and below we list through the third-order coefficients,

$$\begin{aligned}
&H[x_j,0] = H(x_j), \quad H[x_j,1] = \frac{H[x_j,0]-H[x_{j-1},0]}{\Delta x},\\
&H[x_j,2] = \frac{H[x_j,1]-H[x_{j-1},1]}{2\Delta x},\\
&H[x_j,3] = \frac{H[x_j,2]-H[x_{j-1},2]}{3\Delta x}.
\end{aligned} \tag{13}$$

Differentiating (12) with respect to x and evaluating it at x_j give the first-order approximation of $H^{(1)+}$ derivative

$$\left(H^{(1)+}(x_j)\right)' = H[x_j,1], \tag{14}$$

where the $(\ )'$ denotes differentiation with respect to x. Next, second-order interpolants are of two kinds involving the points (x_{j-2}, x_{j-1}, x_j) and (x_{j-1}, x_j, x_{j+1}). In other words, we define

$$\begin{aligned}
&H_1^{(2)+}(x) = H[x_{j-2},0] + H[x_{j-1},1](x-x_{j-2}) + H[x_j,2](x-x_{j-2})(x-x_{j-1})\\
&H_2^{(2)+}(x) = H[x_{j-1},0] + H[x_j,1](x-x_{j-1}) + H[x_{j+1},2](x-x_{j-1})(x-x_j).
\end{aligned} \tag{15}$$

As in the first-order case, we evaluate the derivative of the second-order interpolants at x_j and find,

$$\begin{aligned}
&\left(H_1^{(2)+}(x_j)\right)' = H[x_{j-1},1] + H[x_j,2](3\Delta x)\,,\\
&\left(H_2^{(2)+}(x_j)\right)' = H[x_j,1] + H[x_{j+1},2](\Delta x).
\end{aligned} \tag{16}$$

We take the convex combination of $\left(H_1^{(2)+}(x_j)\right)'$ and $\left(H_2^{(2)+}(x_j)\right)'$, which is "closest" to the lower order approximation, $\left(H^{(1)+}(x_j)\right)'$. So the second-order interpolant based on this decision process is found as $\big(H^{(2)+}(x_j)\big)'$, or it is identical to the upwind (+) portion of the full local Lax–Friedrichs flux in (8),

$$f^{(2)+}_{j+\frac{1}{2}}(u_j) = \frac{1}{2}(f(u_j) + \alpha_{j+\frac{1}{2}}u_j) + \frac{1}{4}(\ell(r_j^+)(\Delta_+ f(u_j) + \alpha_{j+\frac{1}{2}}\Delta_+ u_j)). \tag{17}$$

At third order, there are three interpolants involving points from $(x_{j-3}, x_{j-2}, x_{j-1}, x_j)$, $(x_{j-2}, x_{j-1}, x_j, x_{j+1})$, to $(x_{j-1}, x_j, x_{j+1}, x_{j+2})$. They are

$$\begin{aligned} H^{(3)+}_1(x) &= H[x_{j-3},0] + H[x_{j-2},1](x - x_{j-3}) + H[x_{j-1},2](x - x_{j-3})(x - x_{j-2}) \\ &\quad + H[x_j,3](x - x_{j-3})(x - x_{j-2})(x - x_{j-1}), \end{aligned} \tag{18}$$

$$\begin{aligned} H^{(3)+}_2(x) &= H[x_{j-2},0] + H[x_{j-1},1](x - x_{j-2}) + H[x_j,2](x - x_{j-2})(x - x_{j-1}) \\ &\quad + H[x_{j+1},3](x - x_{j-2})(x - x_{j-1})(x - x_j), \end{aligned} \tag{19}$$

$$\begin{aligned} H^{(3)+}_3(x) &= H[x_{j-1},0] + H[x_j,1](x - x_{j-1}) + H[x_{j+1},2](x - x_{j-1})(x - x_j) \\ &\quad + H[x_{j+2},3](x - x_{j-1})(x - x_j)(x - x_{j+1}), \end{aligned} \tag{20}$$

whose derivatives evaluated at x_j become

$$\left(H^{(3)+}_1(x_j)\right)' = H[x_{j-2},1] + H[x_{j-1},2](5\Delta x) + H[x_j,3](11(\Delta x)^2), \tag{21}$$

$$\left(H^{(3)+}_2(x_j)\right)' = H[x_{j-1},1] + H[x_j,2](3\Delta x) + H[x_{j+1},3](2(\Delta x)^2), \tag{22}$$

$$\left(H^{(3)+}_3(x_j)\right)' = H[x_j,1] + H[x_{j+1},2](\Delta x) + H[x_{j+2},3](-(\Delta x)^2). \tag{23}$$

The convex-weighted differences are tabulated for third order ($n = 3$) involving three possible interpolants labeled $\nu = 1 \ldots 3$ as follows:

$$\begin{gathered} d_1 = c_1(\left(H^{(3)+}_1(x_j)\right)' - \big(H^{(2)+}(x_j)\big)'),\ d_2 = c_2(\left(H^{(3)+}_2(x_j)\right)' - \big(H^{(2)'+}(x_j)\big)'), \\ d_3 = c_3(\left(H^{(3)+}_3(x_j)\right)' - \big(H^{(2)+}(x_j)\big)'). \end{gathered} \tag{24}$$

If all are of the same sign, we find the smallest of these difference and denote it $d_{\nu 0}$ with

$$(H^{(3)+}(x_j))' = \left(H^{(3)+}_{\nu 0}(x_j)\right)'. \tag{25}$$

Otherwise, the lower ordered interpolant is chosen so that

$$(H^{(3)+}(x_j))' = (H^{(2)+}(x_j))'. \tag{26}$$

Values of c_ν are $c_1 = 1.0, c_2 = 0.7, c_3 = 1.0$ for third order. The fourth order interpolant can be constructed in a similar manner, and the coefficients for fourth order are $c_1 = 1.0, c_2 = 0.7, c_3 = 0.7, c_4 = 1.0$.

Thus we can construct the fourth-order local Lax–Friedrichs flux by adding the upwind portion as outlined above and the downwind portion analogously derived:

$$\hat{f}_{j+\frac{1}{2}} = (H^+(x_j))' + (H^-(x_{j+1}))'. \tag{27}$$

Substituting this into (4) sets up the differential equations for the Runge–Kutta scheme discussed in the previous section.

2.3. Equation of motion for propagating interface

A level-set function provides a simple way to track material interfaces and contact surfaces that divide two different media (or materials). We will consider two main types of multi-material interfaces, namely, material–material contact, and material–void (or vacuum) interface. We show how to treat jumps in state variables that are discontinuous, like the density.

The level-set equation,

$$\frac{\partial \phi}{\partial t} + v_1 \frac{\partial \phi}{\partial x} + v_2 \frac{\partial \phi}{\partial y} = 0, \tag{28}$$

is used to track the location of the material interface represented by the zero-level contour $\phi(x, y) = 0$. Initially, we take ϕ to be the signed normal distance function to the interface. The material interface evolves with the local material velocity $\boldsymbol{v} = (v_1, v_2)$. The material velocity on either side of the interface provides the velocity extension that is used for advection of ϕ in the level-set domain. The level-set function, ϕ, is taken positive outside of material and negative inside, and ϕ is initialized to be the signed normal distance from the material interface.

2.4. Material–material interface tracking

Across the contact surface of any two fluids or solids, pressure and velocity are smooth while entropy (likewise density or internal energy) and other material properties may change sharply. This is especially burdensome when numerically solving the equations of motion at an internal boundary. In most finite-difference schemes, either the computed density profile is widely dissipated or spurious oscillations that are associated with the well known 'over-heating' effects are observed [12], [13].

In the case of any two materials (either fluid or solid) in contact, we use a standard pressure update in each region based on the sign of the level-set function. For example, suppose we consider two different ideal gases with distinct γ's in a shock tube. The initial jump in pressure is responsible for the formation of shock and expansion fan, separated by a material contact line. First, the Euler equations are solved simultaneously with the level-set equation, $\phi_t + v\,\phi_x = 0$. The new location of a zero level set is determined as ϕ is propagated with the particle velocity v as a smooth function without discontinuity. The ideal EOS is used to update the pressures on each side of gases with γ taken as $\gamma(\phi)$, with $\gamma = \gamma_1$ if $\phi < 0$, $\gamma = \gamma_2$ if $\phi > 0$, and $\gamma = (\gamma_1 + \gamma_2)/2$ if $\phi = 0$.

In the case of a gas in contact with a metal, the material interface is tracked in

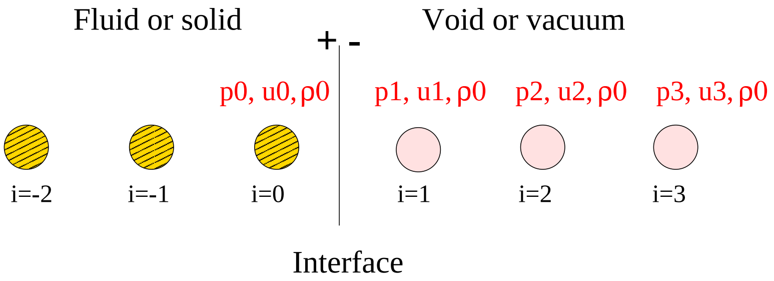

Figure 1. Schematic of material–void interface.

the same way as explained in the ideal gas–gas case. Suppose that we replace one ideal gas with a non-ideal (Mie–Gruneisen) EOS that defines the hydrodynamic EOS for a metal. Then the equations are solved with $p = p_{ideal}$ if $\phi \leq 0$ and $p = p_{M-G}$ otherwise.

2.5. Material–void, stress-free interface tracking

Some examples of material–void contact include the interface between gas and a vacuum, and solid and a void. For both of these cases, the stress-free condition must be satisfied at the interface. Ideally, the zero density and zero stress characterize a vacuum. However, the resulting large density ratio between vacuum and a material puts a significant constraint on any solver, often leading to an early termination of computation and/or unstable marching in both space and time.

We use a modified version of the ghost-fluid-method described in [14] for the general two-material interface for the material–void contact. Experience tells us that a typical density variation across this type of interface is on the order of 10^3. Large oscillations or a smeared out profiles of density are typically observed if a standard pressure update (as shown in section 2.4) is used. One avoids inaccuracies associated with ill-conditioned methods with a one-sided extrapolation of density (or entropy) inside the solid into the vacuum region. Fig. 1 shows how a band of ghost nodes (e.g.

$i = 1 \cdots 3$) that are populated by the first-order extrapolation in one dimension. Using the fact that both pressure and velocity across the material interface (or equivalently a contact line in gas) are smooth and continuous while the density or the entropy usually jumps, we extrapolate the discontinuous density field by assigning $\rho_{i=0}$ into $\rho_{i=1 \cdots 3}$. The ghost zones, now have the pressure and velocity of voids while the density is assigned as the extrapolated density value of the material in contact. Clearly, solving the equation of motion in the new material-ghost zones is easier since the entire field is smooth without any discontinuities. As the level-set function is solved, the interface at $\phi = 0$ position is advected with the particle velocity, and the location of material contact line can be accurately tracked.

At first, this simple technique might seem troublesome because the resulting flow field looks different from the actual physical situation where a solid is in contact with a void. The ideal equation of state for gas or Mie–Gruneisen equation of state for elasto–plastic metals when plotted on e–ρ axes, represents a hyperbola for a specified pressure. These curves with constant pressures are essentially isobars representing different states for gas or metal. So the idea of 'modifying' the density or the internal energy of voids while the pressure remains constant suggests that we are shifting from a point on this isobar to a different point with the density of actual material that corresponds to its internal energy. This technique is an isobaric fix, and is the one used to solve the 'over-heating' problems of piston–gas interface in Ref. [15].

In 2-D, the one-sided extrapolation involves solving the false-transient PDE

$$\frac{\partial I}{\partial \tau} \pm n_x \frac{\partial I}{\partial x} \pm n_y \frac{\partial I}{\partial y} = 0, \tag{29}$$

where I is ρ or e. The unit normal vector $\boldsymbol{n}$ is

$$\boldsymbol{n} = \frac{\nabla\phi}{|\nabla\phi|}. \tag{30}$$

When $\partial I/\partial\tau = 0$, (29) reduces to $\boldsymbol{n}\cdot\nabla I = 0$, which implies that the gradient of I normal to the interface is equal to zero. In practice, one does not solve to steady state; instead, one takes a few steps in $\Delta\tau$ until $\tau > \max(\Delta x, \Delta y)$. A thin band of populated ghost nodes (e.g. $i = 1\cdots 3$) is created by this simple procedure. We choose the + sign in (29) to populate the ghost nodes in the region where $\phi < 0$ with the values of I from the region where $\phi > 0$. Similarly, we choose the - sign in the PDE to populate the ghost nodes in the region where $\phi \geq 0$.

3. Equations

3.1. Euler (inert) equations of compressible flow

The standard equations of motions for compressible flow are the Euler equations,

$$\begin{aligned} \dot{\rho} &+ \rho\nabla\cdot(\boldsymbol{v}) = 0\,,\\ \rho\dot{\boldsymbol{v}} &= -\nabla p\,,\\ \rho\dot{E} &= -\nabla\cdot(p\boldsymbol{v})\,, \end{aligned} \tag{31}$$

with $\rho, \boldsymbol{v}, E$, and p representing the density, velocity vector, total energy per unit mass ($E = e + 1/2\boldsymbol{v}\cdot\boldsymbol{v}$), and the hydrostatic pressure. The hydrodynamic EOS allows us to write the pressure in terms of internal energy and density as $p = p(e,\rho)$.

3.2. Reactive Euler equations

The standard combustion model, for a pre-mixed mixture that can burn, can be derived from a simple mixture theory [16, 17]. The extent of chemical reaction, λ, represents a product mass fraction. One assumes that there are only two distinct species, Fuel and Product. The corresponding chemical reaction is written as $F \rightarrow P + heat$, where the heat of reaction is Q_c.

The balance laws of mass, momentum, and energy are unchanged from (31). In addition, we invoke an evolution law for the reaction progress variable λ,

$$\dot{\lambda} = \Omega, \tag{32}$$

where we have assumed no species diffusion. The hydrodynamic EOS explicitly incorporates exothermic energy release with $\Omega > 0$ and $Q_c > 0$. The ABS model uses the ideal EOS for high-explosive (HE),

$$\rho e = \frac{p}{(\gamma - 1)} - \rho Q_c \lambda \,, \tag{33}$$

with the special rate-law

$$\Omega = H(p^*) A (1 - \lambda)^{1/2} \tag{34}$$

where the rate constant A is chosen to mimic a typical condensed high explosive with $\gamma = 3$, $Q_c = 4 \times 10^6 \, \mathrm{m}^2/\mathrm{s}^2$, and A is given by $2.5147 \times 10^6 \, \mathrm{sec}^{-1}$. The Heaviside function, $H(p^*)$, with $p^* = 1$ GPa is used to prevent any premature reaction ahead of the shock. The steady one-dimensional reaction zone length for a CJ detonation is equal to 4 mm.

3.2.1. Summary of equations for numerical simulation We list a summary of the model equations that are suitable for numerical integration of the two-dimensional, conservative hyperbolic equations. The reactive Euler equations corresponding to (1) have

$$\boldsymbol{U} = \begin{bmatrix} \rho \\ \rho v_1 \\ \rho v_2 \\ \rho E \\ \rho\lambda \end{bmatrix}, \boldsymbol{F} = \begin{bmatrix} \rho v_1 \\ \rho v_1^2 + p \\ \rho v_1 v_2 \\ v_1(\rho E + p) \\ \rho v_1 \lambda \end{bmatrix}, \boldsymbol{G} = \begin{bmatrix} \rho v_2 \\ \rho v_1 v_2 \\ \rho v_2^2 + p \\ v_2(\rho E + p) \\ \rho v_2 \lambda \end{bmatrix} \tag{35}$$

with source

$$\boldsymbol{S} = \begin{bmatrix} 0 \\ 0 \\ 0 \\ 0 \\ \rho\Omega \end{bmatrix}. \tag{36}$$

The ideal EOS for reactive gas with λ representative of the extent of chemical reaction is given by

$$p = (1-\gamma)\left\{\rho E - \frac{\rho}{2}\left(v_1^2 + v_2^2\right) + \rho Q_c \lambda\right\}. \tag{37}$$

3.3. Elasto-plasticity equations for ductile metals

Next, we state a version of the governing equations that can be used to model elasto–plastic solids under high impact loadings. Based on classical incremental small-strain theory [18], we derive an additional scalar evolution law for the effective plastic strain.

The conservation equations follow the formulation of Euler equations of previous section, namely

$$\begin{aligned} \dot{\rho} \quad + \rho\nabla \cdot (\boldsymbol{v}) &= 0\,, \\ \rho\dot{\boldsymbol{v}} &= -\nabla p + \nabla \cdot \boldsymbol{s}\,, \\ \rho\dot{E} + \nabla \cdot (p\boldsymbol{v}) &= \nabla \cdot (\boldsymbol{s}\boldsymbol{v})\,, \end{aligned} \tag{38}$$

where $\rho, \boldsymbol{v}, p, E$ are the same as those defined in (31), while the deviatoric stress $\boldsymbol{s}$ is introduced. The Cauchy stress, defined in the spatial configuration, is $\boldsymbol{\sigma} = \boldsymbol{s} - p\boldsymbol{I}$ so that the stress may consist of a volumetric term (namely a hydrostatic pressure p) and a deviatoric (or traceless) part.

Similar to the equations for compressible gas, the governing laws of motion for solid (here a metal) have additional unknowns which are not defined by these equations. In standard hydrocode formulations, the pressure is defined by hydrodynamic form EOS for metal, which is typically of the Mie–Gruneisen form

$$p = \frac{c_0^2(V_0 - V)}{[V_0 - s(V_0 - V)]^2} + \Gamma_0 \rho_0 V \left\{ \rho e - \frac{\rho}{2} \left(\frac{c_0(V_0 - V)}{V_0 - s(V_0 - V)} \right)^2 \right\} . \tag{39}$$

This EOS is sometimes referred to as the 'U_p–U_s' equation of state. It uses the Rankine-Hugoniot shock relations, and it is required to be consistent with the experimentally measured Hugoniot curve of the form, $U_p = c_0 + s\,U_s$, where U_p is the particle velocity and U_s is shock velocity. The constants c_0 and s are experimentally determined by a straight line fit to the data. Γ_0 is the Mie–Gruneisen coefficient and $V = 1/\rho$. Additional evolution laws are needed to solve for the otherwise undetermined components of deviatoric stress. We next give a brief review of a typical formulation, based on a reasonably standard treatment of metal plasticity.

3.3.1. Derivation of evolution laws of plasticity The overall goal is to express the stress or rate of change of stress given the current stress, a measure of current deformation, deformation rate, and a measure of the history of deformation. From the classical small-strain theory of elasticity, the components of deviatoric stress s_{ij} are expressed in terms of elastic small strain, as

$$s_{ij} \;=\; 2\mu(\hat{\epsilon}_{ij} - \frac{1}{3}\hat{\epsilon}_{kk}\,\delta_{ij}) \;=\; 2\mu\,\hat{\epsilon}'_{ij} \tag{40}$$

where the primed (') notation represents the deviatoric part. The total strain increment $d\boldsymbol{\epsilon}$ is taken to be the sum of elastic and plastic strain:

$$d\boldsymbol{\epsilon} = d\hat{\boldsymbol{\epsilon}} + d\boldsymbol{\epsilon}^p. \tag{41}$$

The corresponding deviatoric incremental strain can be expressed as

$$d\boldsymbol{\epsilon}' = d\hat{\boldsymbol{\epsilon}}' + d\boldsymbol{\epsilon}^p \tag{42}$$

where we use a plastic flow rule to replace $d\boldsymbol{\epsilon}^{p'}$ with $d\boldsymbol{\epsilon}^p$ by using the fact $\epsilon^p_{kk} = 0$. We will give a flow rule below. From (40), the incremental deviatoric stress can be written as

$$d\boldsymbol{s} = 2\mu(d\boldsymbol{\epsilon}' - d\boldsymbol{\epsilon}^p). \tag{43}$$

A yield surface $f(\boldsymbol{\sigma}, \bar{\epsilon}^p)$ is defined by

$$f = \bar{\sigma}(\boldsymbol{\sigma}) - H(\bar{\epsilon}^p) \ = \ 0, \tag{44}$$

where $\bar{\sigma}$ and H represent the effective stress and hardening function, respectively. Equation (44) describes a surface in stress space, where inside of the surface (i.e. $f < 0$) is the elastic region. Yield and subsequent plastic flow take place on the surface ($f = 0$). On the yield surface, f is constant so that

$$df \ = \ \frac{\partial f}{\partial \boldsymbol{\sigma}} : d\boldsymbol{\sigma} + \frac{\partial f}{\partial \bar{\epsilon}^p} d\bar{\epsilon}^p \ = \ \frac{\partial \bar{\sigma}}{\partial \boldsymbol{\sigma}} : d\boldsymbol{\sigma} - \frac{\partial H}{\partial \bar{\epsilon}^p} d\bar{\epsilon}^p \ = \ 0.$$

Upon rearranging, we have the condition for incipient plastic loading

$$\frac{\partial \bar{\sigma}}{\partial \boldsymbol{\sigma}} : d\boldsymbol{\sigma} = \frac{\partial H}{\partial \bar{\epsilon}^p} d\bar{\epsilon}^p. \tag{45}$$

In order to evaluate the derivative of effective stress with respect to the Cauchy stress, the von Mises stress, $\bar{\sigma} = \sqrt{\frac{3}{2}\boldsymbol{s} : \boldsymbol{s}}$, is used so that upon evaluating the derivative, $\partial\bar{\sigma}/\partial\boldsymbol{\sigma}$, (45) becomes

$$\frac{3}{2\bar{\sigma}}\boldsymbol{s} : d\boldsymbol{\sigma} = H' d\bar{\epsilon}^p \quad (\text{using } H' = dH/d\bar{\epsilon}^p). \tag{46}$$

Using the fact that $\boldsymbol{s} : d\boldsymbol{\sigma} = \boldsymbol{s} : d\boldsymbol{s}$, we may write (46) as

$$\frac{3}{2\bar{\sigma}}\boldsymbol{s} : d\boldsymbol{s} = H' d\bar{\epsilon}^p. \tag{47}$$

Using (43) to substitute for $d\boldsymbol{s}$, we obtain

$$\frac{3}{2}\frac{s_{ij}}{\bar{\sigma}} 2\mu(d\epsilon'_{ij} - d\epsilon^p_{ij}) = H' d\bar{\epsilon}^p. \tag{48}$$

In order to derive an equation for the incremental effective plastic strain $d\bar{\epsilon}^p$, we introduce the plastic flow rule based on the plastic potential theory by von Mises. Similar to the elastic potential theory, where the elastic strain is obtained by the derivative of strain energy with respect to Cauchy stress $\boldsymbol{\sigma}$, the incremental plastic strain is

$$\dot{\epsilon}^p_{ij} = \dot{\bar{\epsilon}}^p \frac{\partial Q(\sigma_{ij})}{\partial \sigma_{ij}},$$

where von Mises proposed a plastic potential function $Q(\sigma_{ij})$ whose gradient is proportional to the plastic strain by a factor of $\dot{\bar{\epsilon}}^p$. A common approach in plasticity theory assumes that $Q(\sigma_{ij}) = f(\sigma_{ij}, \bar{\epsilon}^p)$, a yield surface. Then, the plastic strain increment is in the direction normal to the yield surface f (since $\frac{\partial f}{\partial \boldsymbol{\sigma}}(\boldsymbol{\sigma}) \perp f(\boldsymbol{\sigma})$). Evaluating $\partial f/\partial\sigma_{ij}$ leads to

$$\dot{\epsilon}^p_{ij} = \frac{3}{2\bar{\sigma}} s_{ij}\, \dot{\bar{\epsilon}}^p$$

which is also an empirically determined plastic flow rule (Levy–Mises equation).

The Levy–Mises equation based on experiments or plastic potential flow theory can be viewed as giving a 'direction' to a scalar, $\dot{\bar{\epsilon}}^p$, so that $\boldsymbol{R}$, as defined by

$$\boldsymbol{R} = \frac{3}{2}\frac{\boldsymbol{s}}{\bar{\sigma}},$$

may represent a direction tensor. Thus we can express the incremental plastic strain $d\epsilon_{ij}^p$ in terms of the effective plastic strain $d\bar{\epsilon}^p$, a scalar, by giving a direction normal to the yield surface $f = 0$:

$$\frac{3}{2}\frac{s_{ij}}{\bar{\sigma}}2\mu(d\epsilon'_{ij} - \frac{3}{2}\frac{s_{ij}}{\bar{\sigma}}d\bar{\epsilon}^p) = H'd\bar{\epsilon}^p. \tag{49}$$

Finally, solving for $d\bar{\epsilon}^p$, we may write

$$d\bar{\epsilon}^p = \frac{1}{1+\frac{H'}{3\mu}}\frac{\boldsymbol{s} : d\boldsymbol{\epsilon}'}{\bar{\sigma}}. \tag{50}$$

In summary, we have derived evolution equations for $\bar{\epsilon}^p$ and $\boldsymbol{s}$ by replacing the increments with material derivative, such that

$$\begin{align}
\dot{\boldsymbol{s}} &= 2\mu\dot{\hat{\boldsymbol{\epsilon}}}' + \boldsymbol{\Omega s} - \boldsymbol{s\Omega} \nonumber \\
&= 2\mu(\dot{\boldsymbol{\epsilon}}' - \dot{\boldsymbol{\epsilon}}^p) + \boldsymbol{\Omega s} - \boldsymbol{s\Omega} \quad \text{(Using } \dot{\boldsymbol{\epsilon}}' = \boldsymbol{D}' \text{)} \nonumber \\
&= 2\mu(\boldsymbol{D}' - \frac{3}{2}\frac{\boldsymbol{s}}{\bar{\sigma}}\dot{\bar{\epsilon}}^p) + \boldsymbol{\Omega s} - \boldsymbol{s\Omega} \tag{51} \\
\dot{\bar{\epsilon}}^p &= \frac{1}{1+\frac{H'}{3\mu}}\frac{\boldsymbol{s} : \boldsymbol{D}'}{\bar{\sigma}}, \tag{52}
\end{align}$$

where Ω_{ij} are the components of spin tensor, defined by

$$\Omega_{ij} \;=\; \frac{1}{2}(v_{i,j} - v_{j,i}).$$

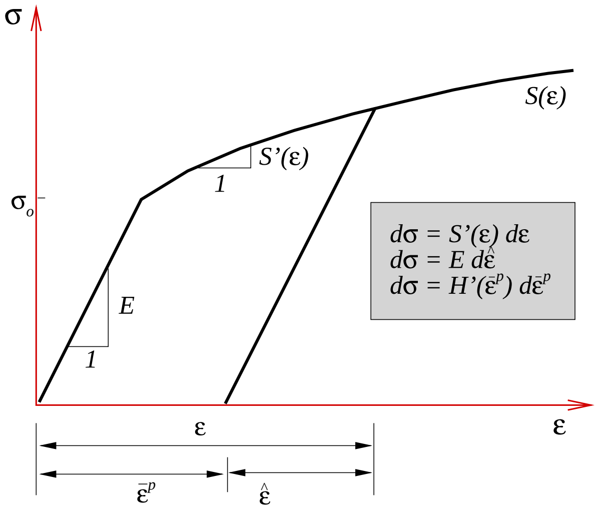

Figure 2. Stress–strain curve from a simple tension test.

The components of deviatoric stretch tensor, D'_{ij}, are defined by

$$D'_{ij} = D_{ij} - \frac{1}{3} D_{kk}\, \delta_{ij} \,,$$

where $D_{ij} = 1/2\,(v_{i,j} + v_{j,i})$. The Ω_{ij} terms in (51) arise because constitutive laws based on Hooke’s law are formulated from objective stress rates as observed in the material frame rotated back to the laboratory frame [19, 2].

3.4. Hardening laws

The simple tension test shown in Fig. 2 illustrates the distinction between the elastic strain $\hat{\epsilon}$ and the effective plastic strain $\bar{\epsilon}^p$, and that summation of the two represents the total natural strain ϵ. Experiments provide a plastic response function $S(\epsilon)$ whose derivative represents a slope of the stress–strain curve $d\sigma/d\epsilon$. As before, a constant elastic slope is denoted E as in Fig. 2. The function $H(\bar{\epsilon}^p)$ is called a hardening function which, in our case of copper, follows an isotropic hardening law. Let

$$H(\bar{\epsilon}^p) = \sigma_o + E_p(\bar{\epsilon}^p)\,\bar{\epsilon}^p \tag{53}$$

where σ_o is a constant yield stress, and $H'(\bar{\epsilon}^p)$ represents the slope of the stress versus effective plastic strain $\bar{\epsilon}^p$ curve. In the case of simple hardening, $H'(\bar{\epsilon}^p) = E_p(\bar{\epsilon}^p)$, a plastic modulus. Noting that S' and E are the slopes of σ–ϵ and σ–$\hat{\epsilon}$ curves, respectively, we can express H' in terms of S' and E:

$$H'(\bar{\epsilon}^p) = \frac{1}{\frac{1}{S'(\epsilon)} - \frac{1}{E}} = \frac{S'(\epsilon)E}{E - S'(\epsilon)}. \tag{54}$$

For classical Taylor anvil impact test for copper, it is sufficient to assume linear hardening. This simplifying assumption allows us to replace $S'(\epsilon)$ with a constant tangent modulus E_t and $H'(\bar{\epsilon}^p)$ with a constant plastic modulus E_p. Table 5 lists the elasto–plastic response properties for a typical copper.

In some extreme ballistic penetration events, a linear hardening of the previous section may not be suitable where the flow stress may exhibit a strong rate-sensitivity. We consider a power law where

$$H(\bar{\epsilon}^p) = \sigma_o \left(1 + \frac{\bar{\epsilon}^p}{\bar{\epsilon}^p_o}\right)^{1/n}. \tag{55}$$

Here, $\bar{\epsilon}^p_o$ is an initial yield strain of a material, and n is the hardening exponent. Johnson and Cook [20] suggest adding the effect of thermal softening to this conventional power law as less plastic behavior is expected of a metal when its temperature is close to the melting point. The hardening law that we use, in addition to the linear relation in (53), takes the following form:

$$H(\bar{\epsilon}^p) = \sigma_o \left[1 - \left(\frac{T - T_o}{T_m - T_o}\right)^{\alpha}\right] \left(1 + \frac{\bar{\epsilon}^p}{\bar{\epsilon}^p_o}\right)^{1/n}, \tag{56}$$

where T_o and T_m are a reference temperature and a melting temperature respectively, and α is the softening exponent. The derivative of the hardening law can be found as

$$H'(\bar{\epsilon}^p) = \frac{\sigma_o}{n\bar{\epsilon}^p_o}\left(1 + \frac{\bar{\epsilon}^p}{\bar{\epsilon}^p_o}\right)^{1/n-1}\left[1 - \left(\frac{T - T_o}{T_m - T_o}\right)^{\alpha}\right]. \tag{57}$$

3.5. Summary of equations of elasto–plasticity for numerical simulation

Now, we can write a form of the elasto–plastic model, similar to hydrodynamic simulation. Here, we treat the deviatoric part of stress as a source term. Based on the hyperbolic equation with source in (38), the conservative variable and spatial fluxes are defined by

$$\boldsymbol{U} = \begin{bmatrix} \rho \\ \rho v_1 \\ \rho v_2 \\ \rho E \\ \rho s_{xx} \\ \rho s_{yy} \\ \rho s_{xy} \\ \rho \bar{\epsilon}^p \end{bmatrix}, \boldsymbol{F} = \begin{bmatrix} \rho v_1 \\ \rho v_1^2 + p \\ \rho v_1 v_2 \\ v_1(\rho E + p) \\ \rho v_1 s_{xx} \\ \rho v_1 s_{yy} \\ \rho v_1 s_{xy} \\ \rho v_1 \bar{\epsilon}^p \end{bmatrix}, \boldsymbol{G} = \begin{bmatrix} \rho v_2 \\ \rho v_1 v_2 \\ \rho v_2^2 + p \\ v_2(\rho E + p) \\ \rho v_2 s_{xx} \\ \rho v_2 s_{yy} \\ \rho v_2 s_{xy} \\ \rho v_2 \bar{\epsilon}^p \end{bmatrix} \tag{58}$$

with source

$$\boldsymbol{S} = \begin{bmatrix} 0 \\ \frac{\partial s_{xx}}{\partial x} + \frac{\partial s_{xy}}{\partial y} \\ \frac{\partial s_{xy}}{\partial x} + \frac{\partial s_{yy}}{\partial y} \\ \frac{\partial}{\partial x}(v_1 s_{xx} + v_2 s_{xy}) + \frac{\partial}{\partial y}(v_1 s_{xy} + v_2 s_{yy}) \\ \rho\left(2\mu\left(D'_{xx} - \frac{3}{2}\frac{s_{xx}}{\bar{\sigma}}\dot{\bar{\epsilon}}^p\right) + \Omega_{xm}s_{mx} - s_{xm}\Omega_{mx}\right) \\ \rho\left(2\mu\left(D'_{yy} - \frac{3}{2}\frac{s_{yy}}{\bar{\sigma}}\dot{\bar{\epsilon}}^p\right) + \Omega_{ym}s_{my} - s_{ym}\Omega_{my}\right) \\ \rho\left(2\mu\left(D'_{xy} - \frac{3}{2}\frac{s_{xy}}{\bar{\sigma}}\dot{\bar{\epsilon}}^p\right) + \Omega_{xm}s_{my} - s_{xm}\Omega_{my}\right) \\ \rho\left(\frac{1}{1+\frac{H'}{3\mu}}\frac{(s_{xx}D'_{xx} + s_{yy}D'_{yy} + 2s_{xy}D'_{xy})}{\bar{\sigma}}\right) \end{bmatrix}, \tag{59}$$

where we have used the definition of Cauchy stress $\boldsymbol{\sigma} = \boldsymbol{s} - p\boldsymbol{I}$ with $s_{xy} = s_{yx}$ and the total energy $\rho E = \rho e + \frac{\rho}{2}(v_1^2 + v_2^2)$. The Mie–Gruneisen EOS (39) is used to represent the pressure behavior of high-strength ductile materials at an elevated pressure ranging in GPa.

Based on the hyperbolic equation with sources (38) in cylindrical coordinates (r, z), the conservative variable and spatial fluxes become

$$\boldsymbol{U} = \begin{bmatrix} \rho \\ \rho v_r \\ \rho v_z \\ \rho E \\ \rho s_{rr} \\ \rho s_{zz} \\ \rho s_{rz} \\ \rho \bar{\epsilon}^p \end{bmatrix}, \boldsymbol{F} = \begin{bmatrix} \rho v_r \\ \rho v_r^2 + p \\ \rho v_r v_z \\ v_r(\rho E + p) \\ \rho v_r s_{rr} \\ \rho v_r s_{zz} \\ \rho v_r s_{rz} \\ \rho v_r \bar{\epsilon}^p \end{bmatrix}, \boldsymbol{G} = \begin{bmatrix} \rho v_z \\ \rho v_r v_z \\ \rho v_z^2 + p \\ v_z(\rho E + p) \\ \rho v_z s_{rr} \\ \rho v_z s_{zz} \\ \rho v_z s_{rz} \\ \rho v_z \bar{\epsilon}^p \end{bmatrix} \tag{60}$$

with source

$$\boldsymbol{S} = \begin{bmatrix} -\frac{\rho v_r}{r} \\ \frac{\partial s_{rr}}{\partial r} + \frac{\partial s_{rz}}{\partial z} + \frac{s_{rr}}{r} \\ \frac{\partial s_{rz}}{\partial r} + \frac{\partial s_{zz}}{\partial z} + \frac{s_{rz}}{r} \\ \frac{\partial}{\partial z}(v_r s_{rr} + v_z s_{rz}) + \frac{\partial}{\partial z}(v_r s_{rz} + v_z s_{zz}) - \frac{p v_r}{r} + \frac{(s_{rr} v_r + s_{rz} v_z)}{r} \\ \rho\left(2\mu\left(D'_{rr} - \frac{3}{2}\frac{s_{rr}}{\bar{\sigma}}\dot{\bar{\epsilon}}^p\right) + \Omega_{rm} s_{mr} - s_{rm}\Omega_{rx}\right) \\ \rho\left(2\mu\left(D'_{zz} - \frac{3}{2}\frac{s_{zz}}{\bar{\sigma}}\dot{\bar{\epsilon}}^p\right) + \Omega_{zm} s_{mz} - s_{zm}\Omega_{mz}\right) \\ \rho\left(2\mu\left(D'_{rz} - \frac{3}{2}\frac{s_{rz}}{\bar{\sigma}}\dot{\bar{\epsilon}}^p\right) + \Omega_{rm} s_{mz} - s_{rm}\Omega_{mz}\right) \\ \rho\left(\frac{1}{1+\frac{H'}{3\mu}}\frac{(s_{rr} D'_{rr} + s_{zz} D'_{zz} + 2 s_{rz} D'_{rz})}{\bar{\sigma}}\right) \end{bmatrix}. \tag{61}$$

4. Code validations

4.1. Time step decision

The time step of the multi-material code is calculated using the CFL condition:

$$\Delta t = CFL \times \min \left\{ \frac{\Delta x}{\max \left| \frac{d\boldsymbol{f}}{d\boldsymbol{u}} \right|}, \frac{\Delta y}{\max \left| \frac{d\boldsymbol{g}}{d\boldsymbol{u}} \right|} \right\} \tag{62}$$

where CFL is the Courant number, $\max \left| \frac{d\boldsymbol{f}}{d\boldsymbol{u}} \right|$ and $\max \left| \frac{d\boldsymbol{g}}{d\boldsymbol{u}} \right|$ are the largest eigenvalues (in absolute sense) of the Jacobians of $\boldsymbol{f}$ and $\boldsymbol{g}$. In order to evaluate the Jacobians, we introduce new variables such as

$$\boldsymbol{u} = \begin{bmatrix} \rho \\ m \\ n \\ r \\ \alpha \\ \beta_i \end{bmatrix} = \begin{bmatrix} \rho \\ \rho v_1 \\ \rho v_2 \\ \rho E \\ \rho \lambda \\ \rho \phi_i \end{bmatrix}, \tag{63}$$

where $i = 1, \ldots,$ and ϕ_i may represent three deviatoric stress components and the effective plastic strain. The conservative fluxes in x, y directions can be expressed by

$$\boldsymbol{f} = \begin{bmatrix} m \\ \frac{m^2}{\rho} + p \\ \frac{mn}{\rho} \\ \frac{m}{\rho}(r+p) \\ \frac{\alpha m}{\rho} \\ \frac{\beta_i m}{\rho} \end{bmatrix}, \quad \boldsymbol{g} = \begin{bmatrix} n \\ \frac{mn}{\rho} \\ \frac{n^2}{\rho} + p \\ \frac{n}{\rho}(r+p) \\ \frac{\alpha n}{\rho} \\ \frac{\beta_i n}{\rho} \end{bmatrix}. \tag{64}$$

Upon evaluating the derivative of $\boldsymbol{f}$ with respect to $\boldsymbol{u}$, we find the Jacobian of $\boldsymbol{f}$ as

$$\frac{d\boldsymbol{f}}{d\boldsymbol{u}} = \begin{bmatrix} 0 & 1 & 0 & 0 & 0 & 0 \\ -\frac{m^2}{\rho^2} + \frac{\partial p}{\partial \rho} & \frac{2m}{\rho} + \frac{\partial p}{\partial m} & \frac{\partial p}{\partial n} & \frac{\partial p}{\partial r} & \frac{\partial p}{\partial \alpha} & \frac{\partial p}{\partial \beta_i} \\ -\frac{mn}{\rho^2} & \frac{n}{\rho} & \frac{m}{\rho} & 0 & 0 & 0 \\ -\frac{m}{\rho^2}(r+p) + \frac{m}{\rho}\left(\frac{\partial p}{\partial \rho}\right) & \frac{(r+p)}{\rho} + \frac{m}{\rho}\left(\frac{\partial p}{\partial m}\right) & \frac{m}{\rho}\left(\frac{\partial p}{\partial n}\right) & \frac{m}{\rho}\left(1 + \frac{\partial p}{\partial r}\right) & \frac{m}{\rho}\frac{\partial p}{\partial \alpha} & \frac{m}{\rho}\frac{\partial p}{\partial \beta_i} \\ -\frac{\alpha m}{\rho^2} & \frac{\alpha}{\rho} & 0 & 0 & \frac{m}{\rho} & 0 \\ -\frac{\beta_i m}{\rho^2} & \frac{\beta_i}{\rho} & 0 & 0 & 0 & \frac{m}{\rho} \end{bmatrix}. \tag{65}$$

The Jacobian of $\boldsymbol{g}$ is found as

$$\frac{d\boldsymbol{g}}{d\boldsymbol{u}} = \begin{bmatrix} 0 & 0 & 1 & 0 & 0 & 0 \\ -\frac{mn}{\rho^2} & \frac{n}{\rho} & \frac{m}{\rho} & 0 & 0 & 0 \\ -\frac{n^2}{\rho^2} + \frac{\partial p}{\partial \rho} & \frac{\partial p}{\partial m} & \frac{2n}{\rho} + \frac{\partial p}{\partial n} & \frac{\partial p}{\partial r} & \frac{\partial p}{\partial \alpha} & \frac{\partial p}{\partial \beta_i} \\ -\frac{n}{\rho^2}(r+p) + \frac{n}{\rho}\left(\frac{\partial p}{\partial \rho}\right) & \frac{n}{\rho}\frac{\partial p}{\partial m} & \frac{(r+p)}{\rho} + \frac{n}{\rho}\left(\frac{\partial p}{\partial n}\right) & \frac{n}{\rho}\left(1 + \frac{\partial p}{\partial r}\right) & \frac{n}{\rho}\frac{\partial p}{\partial \alpha} & \frac{n}{\rho}\frac{\partial p}{\partial \beta_i} \\ -\frac{\alpha n}{\rho^2} & 0 & \frac{\alpha}{\rho} & 0 & \frac{n}{\rho} & 0 \\ -\frac{\beta_i n}{\rho^2} & 0 & \frac{\beta_i}{\rho} & 0 & 0 & \frac{n}{\rho} \end{bmatrix}. \quad (66)$$

The eigenvalues of the Jacobians (65) and (66) are

$$\lambda^f = v_1 - c, v_1, v_1, v_1, v_1, v_1 + c \quad (67)$$

$$\lambda^g = v_2 - c, v_2, v_2, v_2, v_2, v_2 + c \quad (68)$$

where c is defined by

$$c^2 = \frac{\partial p}{\partial \rho} + \frac{p}{\rho}\frac{\partial p}{\partial r}. \quad (69)$$

The partial derivatives of p can be evaluated for a given EOS. In the case of an ideal EOS, $p = (\gamma - 1)(r - \frac{1}{2\rho}(m^2 + n^2))$, the partial derivatives are

$$\frac{\partial p}{\partial \rho} = (\gamma - 1)\frac{1}{2\rho^2}(m^2 + n^2), \quad \frac{\partial p}{\partial m} = -(\gamma - 1)\frac{m}{\rho}, \quad \frac{\partial p}{\partial n} = -(\gamma - 1)\frac{n}{\rho},$$
$$\frac{\partial p}{\partial r} = \gamma - 1, \quad \frac{\partial p}{\partial \alpha} = 0, \quad \frac{\partial p}{\partial \beta_i} = 0. \quad (70)$$

For an ideal EOS for high-explosive (HE), $p = (\gamma - 1)(r + Q_c\alpha - \frac{1}{2\rho}(m^2 + n^2))$, where Q_c is a heat of combustion, the partial derivatives of pressure are

$$\frac{\partial p}{\partial \rho} = (\gamma - 1)\frac{1}{2\rho^2}(m^2 + n^2), \quad \frac{\partial p}{\partial m} = -(\gamma - 1)\frac{m}{\rho}, \quad \frac{\partial p}{\partial n} = -(\gamma - 1)\frac{n}{\rho},$$
$$\frac{\partial p}{\partial r} = \gamma - 1, \quad \frac{\partial p}{\partial \alpha} = (\gamma - 1)Q_c, \quad \frac{\partial p}{\partial \beta_i} = 0. \quad (71)$$

In the case of Mie–Gruneisen EOS, the pressure is given by

Table 1. Initial parameters of shock tube Case A.

	Gas1 (50 cm)	Gas2 (50 cm)
γ	1.4	1.2
ρ (kg/m^3)	1	0.125
p (Pa)	1.5×10^5	1.0×10^4
v (m/s)	0	0

$$p = \frac{c_o^2(V_o - \frac{1}{\rho})}{[V_o - s(V_o - \frac{1}{\rho})]^2} + \frac{\Gamma_o}{V_o\rho}\left\{ r - \frac{1}{2\rho}(m^2 + n^2) - \frac{\rho}{2}\left(\frac{c_o(V_o - \frac{1}{\rho})}{V_o - s(V_o - \frac{1}{\rho})}\right)^2 \right\}. \tag{72}$$

The partial derivatives of pressure become

$$\frac{\partial p}{\partial \rho} = \frac{c_o\rho^3V_o(s - \rho V_o - \rho s V_o) + \Gamma\left(n^2(C_1)^3 + m^2(C_1)^3 + \rho(c_o^2\rho^2V_o(-1 + \rho V_o) - r(C_1)^3)\right)}{\rho^3V_o(C_1)^3}$$

$$\frac{\partial p}{\partial m} = -\frac{\Gamma}{V_o\rho^2}m, \quad \frac{\partial p}{\partial n} = -\frac{\Gamma}{V_o\rho^2}n, \quad \frac{\partial p}{\partial r} = \frac{\Gamma}{V_o\rho}, \quad \frac{\partial p}{\partial \alpha} = 0, \quad \frac{\partial p}{\partial \beta_i} = 0 \tag{73}$$

with $C_1 = \rho V_o - s + \rho s V_o$.

So, the optimal time step (62) can be computed by picking the larger of the eigenvalues in λ_f and λ_g. This procedure will assure that the domain of influence is properly covered by the computational mesh in space–time.

4.2. Verification of order of convergence

As a first test, we consider two different Euler gases initially brought to contact. Upon the removal of the diaphragm between the gases with different γ's, an expansion wave and a normal shock propagate in the opposite direction, and a contact surface (or material interface) follows the right-running shock. Listed in Table 1 are the initial conditions of this experiment.

Figure 3 shows the result calculated with 100 points spanning 1 meter in the x direction. We used the fourth-order convex ENO scheme with a third-order Runge–

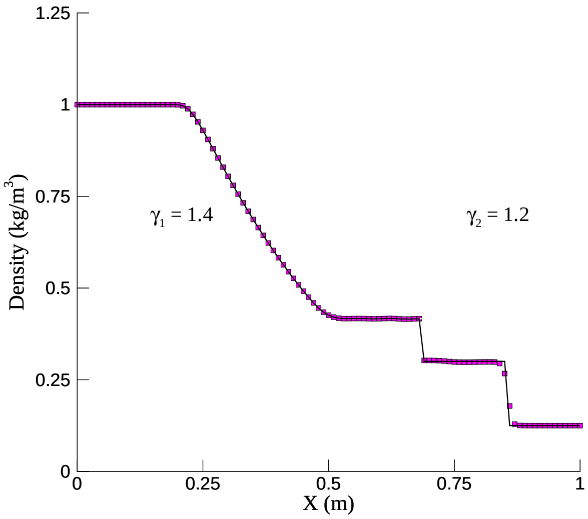

Case A

Figure 3. Riemann problem involving two different gases used in the validation of rate of numerical convergence.

Kutta scheme scheme described in section 2.1. The material interface or the contact line between the gases are tracked via the level-set approach using the one-sided extrapolation of density as discussed in section 2.5. We note that there is essentially no smearing across the material interface.

We analyze the spatial accuracy by measuring the relative error E_1 in the L_1 norm during the time integration to estimate the order of convergence similar to Ref. [21]. The eight data points (e.g. density) between $x = 0.52$ to $x = 0.59$ in increments of $\Delta x = 0.01$ are compared with the double grid data points at the same locations at time $t = 0.0007$. The discrete L_1 norm is defined as

$$E_1 = \sum_i |\rho^{\text{exact}} - \rho_i|\Delta x. \tag{74}$$

If a method is of r th order, then for a uniform mesh with N grid points, the error

Table 2. Results of numerical test of convergence. In the table, N denotes grid points, E_1 is the L_1 norm of error measured between the grids of size N and $2N$ points, and r_c is the rate of convergence.

N	E_1	r_c
100	9.0×10^{-5}	—
200	1.68×10^{-5}	2.4
400	2.7×10^{-6}	2.8
800	1.8×10^{-7}	3.9

should satisfy

$$E_1^N = O(\Delta x^{r_c}).$$

When the uniform mesh is refined by doubling the grid points, we should have

$$E_1^{2N} = O\left(\left(\frac{\Delta x}{2}\right)^{r_c}\right).$$

Then, one can solve for the rate of convergence, r_c, and finds

$$r_c = \frac{\ln E_1^N - \ln E_1^{2N}}{\ln 2}. \tag{75}$$

The L_1 error and the rate of convergence based on density are displayed in Table 2 with the rate of convergence calculated from (75). The fourth-order convex ENO scheme, combined with the level-set representation of the material interface, is tested in this 1-D shock tube exercise. Clearly, as the grids are refined we observe that the computed rate of convergence approaches the theoretical value of 4. Here, we make sure that Δt is kept small compared with Δx to make sure that no additional errors are coming from the third-order temporal scheme, which will hinder the approach to the theoretical convergence rate of 4.

Table 3. Initial parameters of shock tube Case B.

	Gas1 (5 cm)	Gas1 (45 cm)	Gas2 (50 cm)
γ	1.4	1.4	1.67
ρ (kg/m^3)	1.333	1.0	0.1379
p (Pa)	1.5×10^5	1.0×10^5	1.0×10^5
v (m/s)	$0.3535\sqrt{10^5}$	0	0

4.3. Validation 1: 1-D shock reflection of two different gases

In the second shock-tube test, we start from a right-running shock that reflects off a contact line at the center of a shock tube consisting of two gases of different γ. A part of the incident shock running from left to right will be transmitted as there is a right-moving interface separating two different shocks running in the opposite direction. The initial conditions are summarized in Table 3.

Figure 4 shows the wave structures inside the tube after some period of time. Upon the incidence of initial shock on the interface originally at $x = 0.5$ m, a part gets transmitted to the right-side gas, and part gets reflected while the interface between the two follows the local particle velocity, moving to the right. The level-set method with and without the one-sided extrapolation accurately captures the location of shocks in opposite directions. Noticeably, the material interface between the two gases is resolved without any smearing in the one-sided extrapolated method while the transmitted and reflected shocks are a bit smeared out by the fourth-order convex ENO scheme.

4.4. Validation 2: ZND structure

We test our multi-dimensional reactive Euler code by checking for the maintenance of a stable 1-D, ZND detonation wave. We show the results of a test, where we took discontinuous initial data with ambient (and motionless) conditions ahead (in

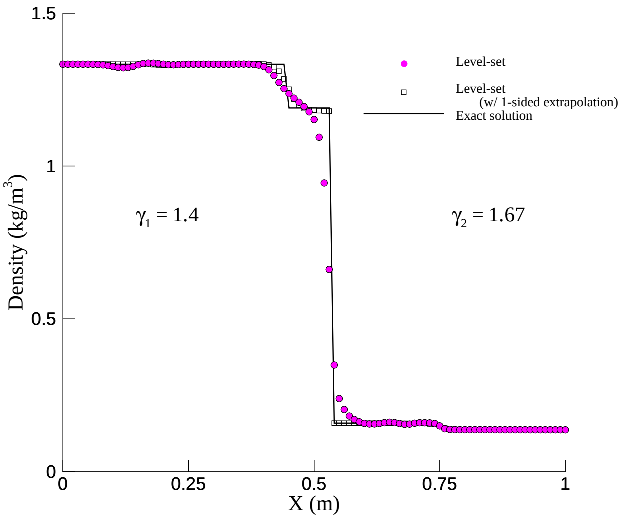

Case B

Figure 4. Multi-material shock-tube test of shock reflection and transmission into two adjacent gases.

Table 4. Initial end states of CJ detonation wave in a typical high-explosive.

	Burnt (CJ)	Fresh
p (Pa)	32×10^9	10^5
ρ (g/cc)	$8/3$	2
v (m/s)	2000	0
γ	3	3
λ	1	0

the positive direction) and constant Chapman–Jouguet (CJ) states behind, for the ABS test case with $\gamma = 3$, $Q_c = 4 \times 10^6\,\mathrm{m}^2/\mathrm{s}^2$, and $A = 2.5147 \times 10^6\,\mathrm{sec}^{-1}$. A steady detonation profile quickly sets up, and the computed steady structure is shown in Fig. 5. The spatial structure perfectly overlays that obtained by integrating the steady ODEs for the ZND structure. The end states of the CJ detonation are listed in Table 4. The computed reaction zone thickness is 4 mm, and the steady CJ detonation propagates at a speed 8.0×10^3 m/s.

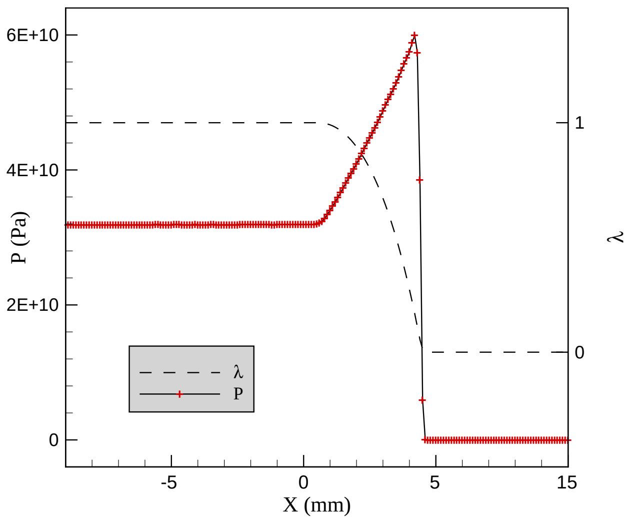

Figure 5. ZND detonation structure calculated by the multi-dimensional reactive Euler solver. Δx is 0.1 mm, and consequently 40 points are placed in the 4 mm reaction zone.

Certainly, it would be beneficial to use extensive meshes in all regions of the flow field without any adaptive meshing effort; however our multi-dimensional computations are for only a limited number of points—about 10 points across the reaction zone, which is deemed to be sufficient to accurately describe the qualitative behavior of the material interactions.

4.5. Validation 3: Taylor anvil test, copper rod impact

A cylindrical rod of initial radius of 3.2 mm and a length of 32.4 mm strikes a rigid wall head-on at a velocity of 227 m/s. The rod is made of copper, and Table 5 summarizes the material properties of copper that are used in our simulation. By comparison of our results with experimental and computational results obtained by others (see [22], [23], [24]), this experiment provides a validation of our model and numerics. For simplicity, we assumed a linear hardening law with a plastic modulus

Table 5. Material properties typical of copper.

Material Property	Value
density of copper	8.930 g/cc
shear modulus (μ)	43.222 GPa
Poisson ratio (ν)	0.35
Young's modulus (E)	117 GPa
plastic modulus (E_p)	100 MPa
yield stress (σ_o)	400 MPa
Mie–Gruneisen coefficient, Γ_o	2.0
Mie–Gruneisen coefficient, s	1.49
speed of sound, c_o	3.94 km/s

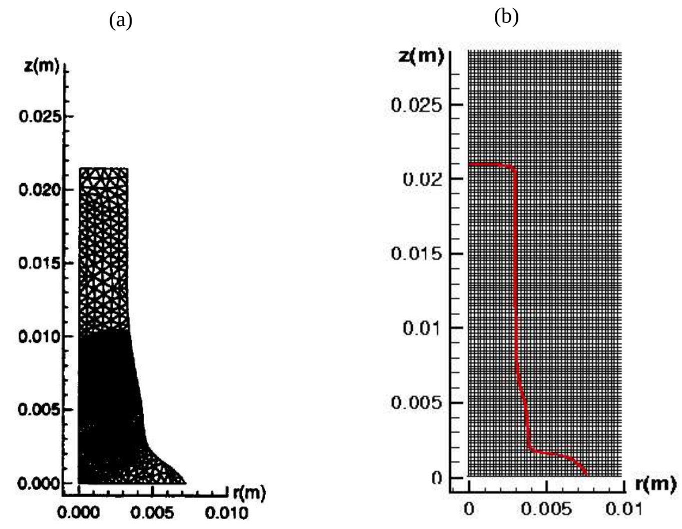

0.6 mm < mesh size < 1.2 mm

Uniform mesh size = 0.2 mm

Figure 6. Grid comparison: (a) deformed grid at time $t = 80\,\mu$sec used in the Lagrangian FEM calculation by [7]; (b) uniform grid used in this work.

of $E_p = 100$ MPa. We expect the final deformed shape, length, and radius to be comparable to a benchmark result. Further, we expect the effective plastic strain field to match reasonably closely. Our simulation was run out to 80 μsec on our eight-processor SGI Origin.

Figures 6 and 7 show on the right, the final deformed shape of our rod on our fixed Cartesian grid used in our Eulerian calculation. The rod is initially traveling

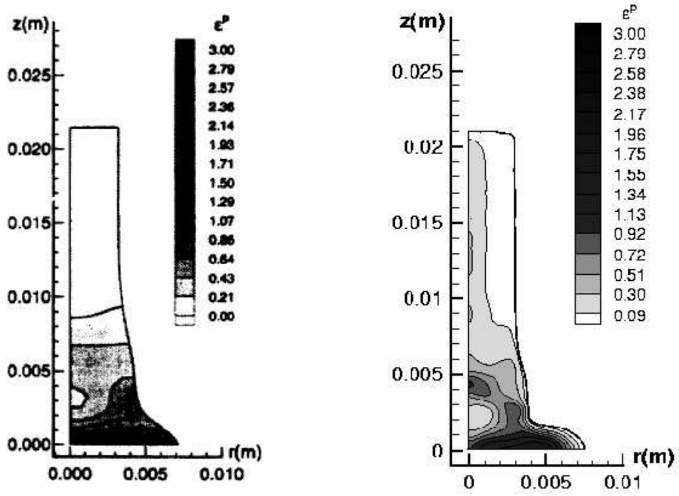

Camacho & Ortiz (1997) **This work**

Figure 7. Comparison of effective plastic strain distribution at 80 μsec. A 50 × 170 grid spans the r and z directions ($\Delta r = \Delta z = 2.0 \times 10^{-4}$m).

with a velocity of 227 m/s directed downward and is initially undeformed. On the left for comparison, the benchmark numerical result computed by Camacho and Ortiz [7]|| is shown at $t = 80\,\mu$sec. They use an adaptive finite element solver on a Lagrangian mesh with a finite-strain plasticity model. Our simulation uses an incremental strain formulation, so the results can be compared qualitatively but are not necessarily expected to be exactly the same. However, our computed results shown on the right-hand side are strikingly similar to their benchmark numerical result, and our computed plastic strain field is almost quantitatively in agreement with their result compared with the maximum value nearing 3. With our code, one can produce animations (not shown) that show the rod decelerating on impact and a shock propagating through the rod to the top with reverberations.

|| Reprinted from Computer Methods in Applied Mechanics and Engineering, Vol 142, Camacho and Ortiz, “Adaptive Lagrangian modelling of ballistic penetration of metallic targets”, pp 269–301, Copyright 1997, with permission from Elsevier Science.

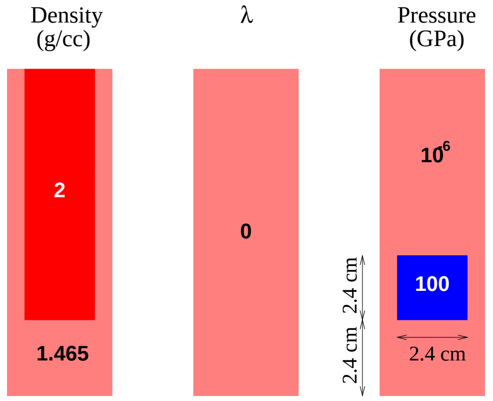

Figure 8. Schematic of the rate-stick experiment of Aslam and Bdzil, [8].

Table 6. Parameter of rate-stick experiment of Ref. [8].

	HE	HE (Booster)	Inert
density (kg/m^3)	2000	2000	1465
pressure (GPa)	10^{-4}	100	10^{-4}
γ	3	3	1.4
λ	0	0	0

4.6. Validation 4: Rate-stick experiment

For our last validation exercise of our multi-material code, we consider a test problem formulated by T. Aslam and J. Bdzil of Los Alamos National Laboratory [8]. A 'stick' of HE of length 36 cm and width 1.2 cm, is initially placed in an inert medium surrounded by an inert layer on the bottom of thickness 2.4 cm and on either side by a thin layer, 0.4 cm thick. Fig. 8 shows the initial setup of the experiment where density, extent of reaction, and pressure fields are shown. A pocket of high-pressure HE of dimension 2.4 by 2.4 cm initiates a steady detonation wave in the y direction and the hot gas pushes the HE–Inert interface outward in the x direction. The parameters for the problem are summarized in Table 6. For their simulation of this experiment, Aslam and Bdzil used a modified form of *Amrita* that uses a high-resolution, patch-based adaptive mesh refinement algorithm [25].

Figure 9 shows comparison of two independently calculated results of rate-stick. The left figures are from Aslam and Bdzil while the right is our result. Aslam's results were computed based on the adaptive grids, which give $\Delta x = \Delta y = 0.0074$ cm or 54 points in the complete reaction zone of thickness 4 mm. The results are based on the uniform mesh of size 0.027 cm, allowing 15 points across the reaction zone. In both fields of λ and ρ, we see an excellent agreement of the detonation front and the angle of shock transmitted into the inert. We match Aslam and Bdzil's steady detonation speed of 6.9 mm/μs.

Even with a coarse grid resolution (i.e. approximately 1/4th of that in Ref. [8]), our multi-material numerics reproduce the fine-grid results of Aslam. With our new code, we simulate multi-material problems with a higher degree of complexity, namely interaction between HE and metals. We will demonstrate its use for applications and in cases where analytical solutions (or experimental simulations) are difficult to obtain for direct comparison.

5. Applications

5.1. HE–Cu–Void (a "challenging" rate-stick) problem

The interface treatment technique as discussed in section 2 is concerned with material–void or material–vacuum contact. We extend this approach to incorporate a generic material–material interface with a simple use of level sets. By tracking two different interfaces, namely the contact interface between a high explosive–copper and copper–void, we use our unified fluid–solid code for complex impact and penetration problems.

A plane steady Chapman–Jouguet (CJ) detonation wave is used as the initial solution at the bottom of a rate-stick shown in the schematic, Fig. 10. Experimental observations for rate-sticks confirm that the steady, curved detonation wave propagates down the axis more slowly than a planar detonation (the diameter

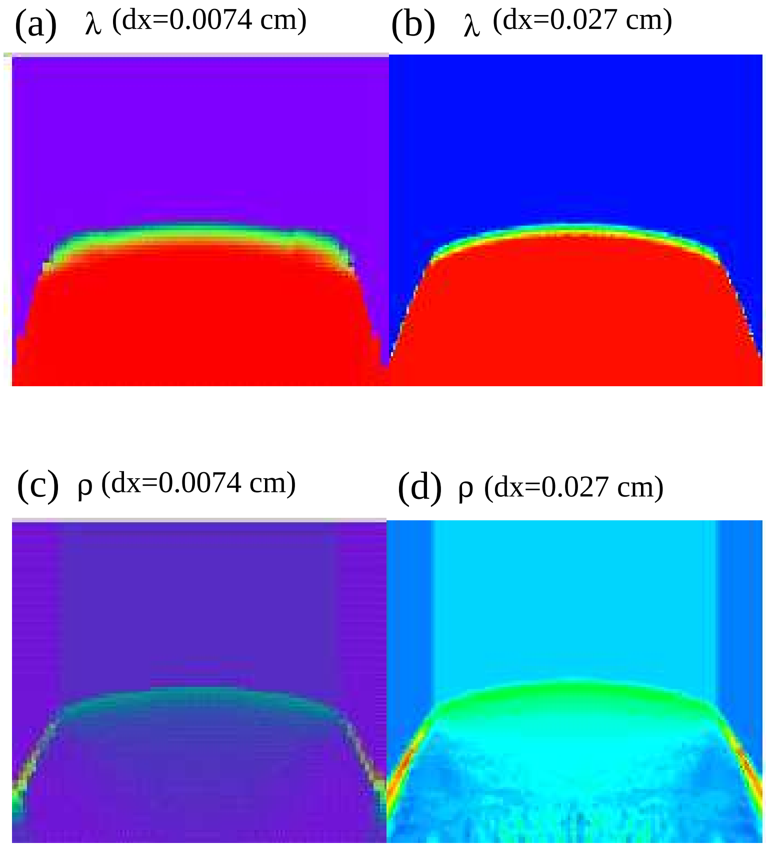

Figure 9. Comparison of the rate-stick simulations. Shown on the left is extent of reaction and density from Ref. [8] with $\Delta x = \Delta y = 0.0074$ cm or 54 points in the reaction zone. The results on the right are computed with $\Delta x = \Delta y = 0.027$ cm or 15 points in the reaction zone.

effect). The axial wave speed varies with the diameter of the stick and also depends on the type of confinement. With a finite thickness of the copper confinement, we can determine the shock angle in the steady propagating wave system and the constant speed.

Figures 11 and 12 show the transient behavior of an initially planar detonation wave that develops into a steady curved detonation that maintains a shock in the copper confinement. The time elapsed between the frames shown in the figure is approximately 5 μsec. The sequence shows that a curved detonation sets up in the

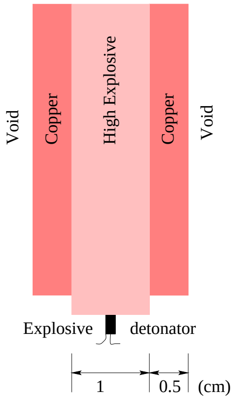

Figure 10. Schematic of a “challenging” rate-stick experiment.

Table 7. Material properties of high-strength steel.

Material Property	Value
density	7.85 g/cc
shear modulus (μ)	77.5 GPa
Poisson ratio (ν)	0.29
Young’s modulus (E)	200 GPa
yield stress (σ_o)	1500 MPa
softening exponent, α	1.17
hardening exponent, n	22
melting temperature, T_m	1777 Kelvin
reference temperature, T_o	300 Kelvin

metal-clad rate stick and propagates steadily.

5.2. Explosive welding

Figure 13 shows a sketch that represents the basic configuration for explosive welding. Initially separated by a small gap, one of two metal plates is coated with a layer of high explosive (HE). A detonator generates a shock wave, which starts a detonation in the HE. The detonation shock drives copper plate into a steel plate (say). The collision generates a shear velocity profile in the vicinity of the copper/steel interface with velocities that are a sizable fraction of the particle velocity in the explosive products, which is about 2000 m/s for a planar, ABS, CJ detonation.

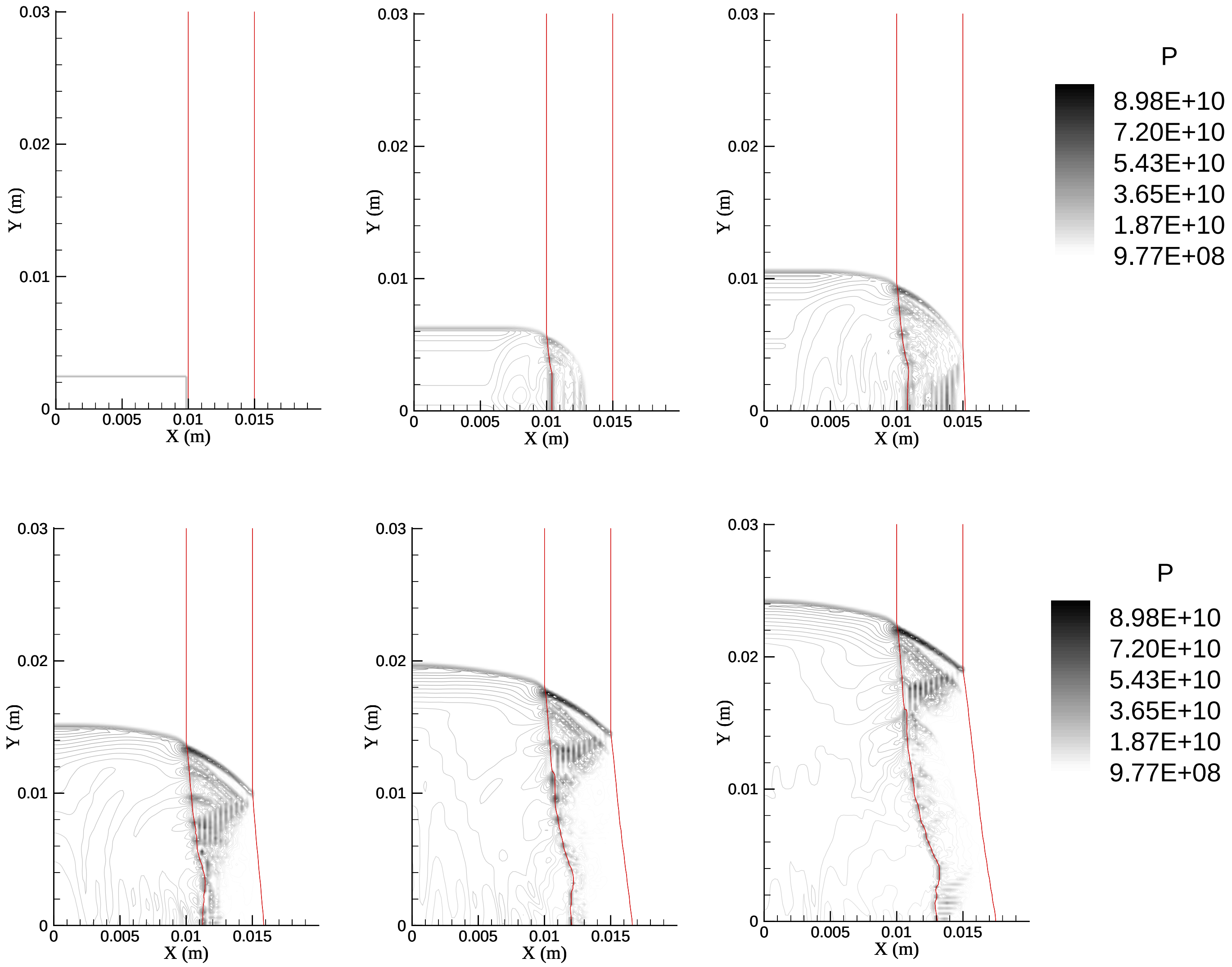

Figure 11. Rate-stick experiment simulated on 100 by 150 grid with 0.5 cm initial thickness copper plate. The pressure field is shown approximately every 5 μsec. The 2 cm-thick cylinder of HE is confined in a 5 mm-thick copper tube. The outside of the copper slab is a free surface.

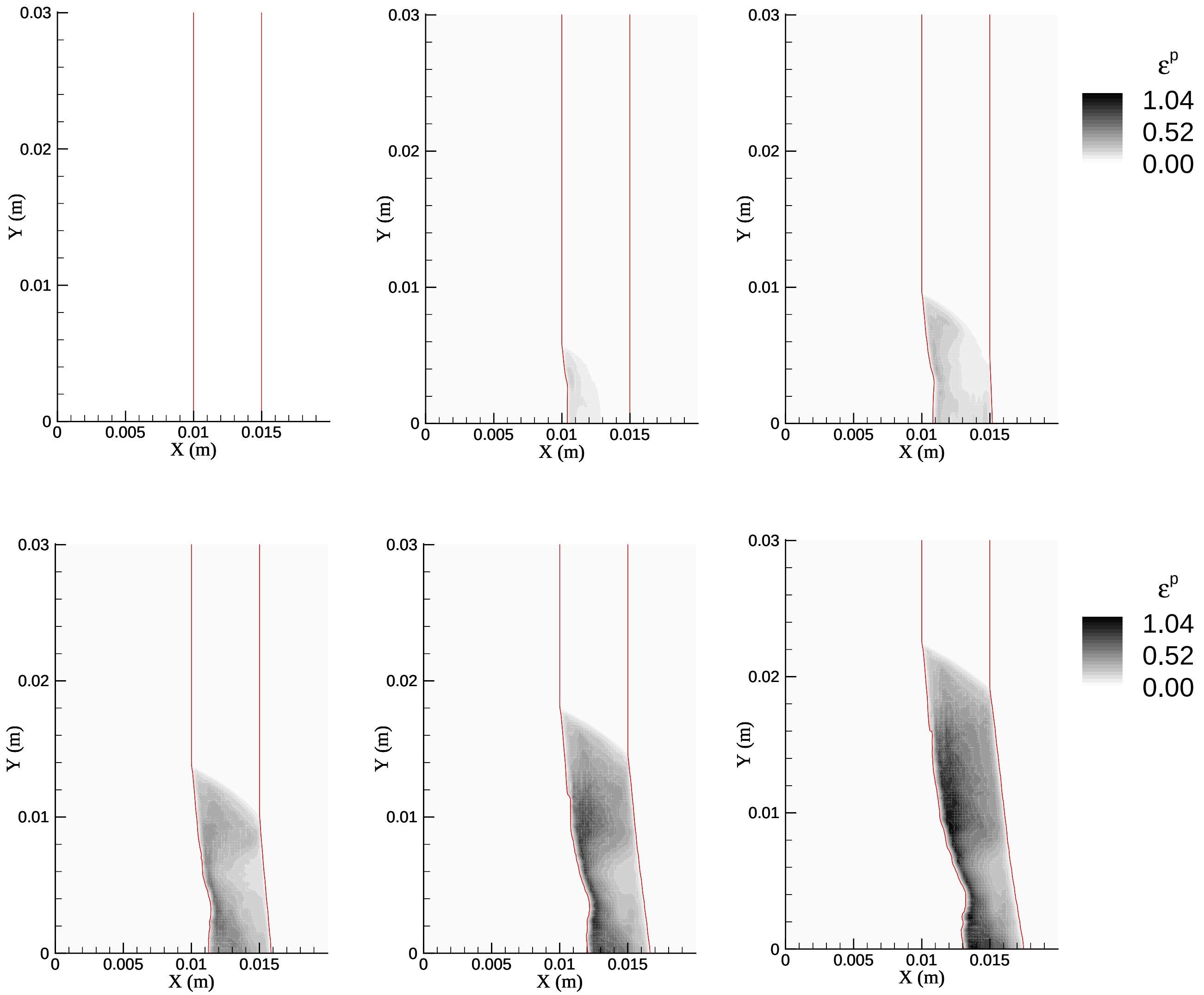

Figure 12. The effective plastic strain field is shown approximately every 5 μsec, for the copper clad rate stick problem.

To simulate the HE–Copper–Steel contact problem in the welding setting, we used a high pressure region in the ABS explosive to initiate the detonation. The high pressure region was placed at the left end with dimensions of 0.2 cm by 1 cm. In addition, to mimic early skew contact, we took the particle velocity in the high pressure block to be 2000 m/s along the plate and (0.087)(2000) m/sec normal to the horizontal plates. In this way, the interface between the HE and the copper plate initially experiences both the shearing and normal velocities just as in the actual experiment shown in Fig. 13.

Numerical results are shown in Figs. 14 and 15. The overlaid lines of the level-set functions on the pressure and the density figures represent the material interfaces between the metals and HE. The interfaces that were initially located at 1 cm and 1.5 cm, move downward due to the action of the initiation and the subsequent propagation of the detonation. Tremendous ringing is observed in the copper plate when the strong shock wave first penetrates and becomes weaker as it is transmitted through the less-dense steel. Since the plastic yielding occurs at a much lower stress state in copper, the hardening behavior (seen as perturbations or 'ringing') is very pronounced in the copper layer. Although the unstable shearing motions are not obvious in the copper–steel interface, this slip line at the interface has the potential to generate a Kelvin–Helmholtz instability, resulting in rolling up of the contact lines. In [6], we considered the shear-induced melting of two plates in contact. The liquid interface between the plates became unstable as the plates experienced a shear motion. By allowing the copper and steel of the welding simulation to undergo phase transformations, we believe that, with a modification of the constitutive model, we can melt the interface and see coherent wavy structures as the unstable interface starts to roll up. However, that simulation is beyond our present scope.

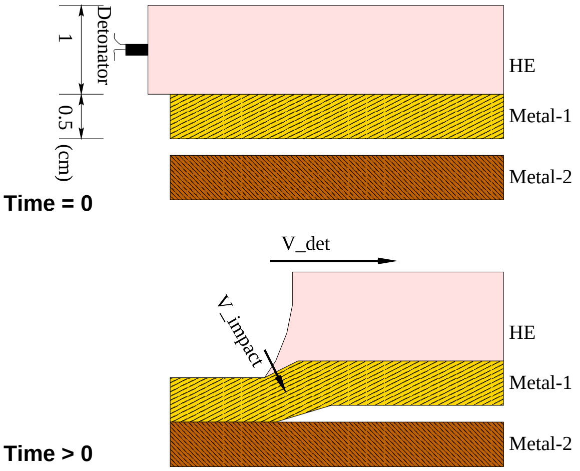

Figure 13. Schematic of explosive welding of two metal plates.

5.3. Impact of copper plate target with a spherical detonation

First, the initial shape and location of two material interfaces are prescribed by a single distance function for each interface:

$$\phi_1 = 1\ \text{cm} - x\,, \quad \phi_2 = (1\ \text{cm} + \ \text{width}) - x\,,$$

where the distance from the left inlet to a first interface is assigned a distance 1 cm, and the width is set 0.5 cm of the initial copper plate thickness. As the hot spot initiates a spherical detonation wave in a radial direction, chemical reaction instantly consumes the fuel and a thin reaction front is coupled to a shock approaching the first interface between the HE–Copper. As the shock penetrates the copper, we see an incipient plastic deformation in the metal as shown in Fig. 17. The highest effective plastic strains are observed where extreme bending occurs right at the center and the upper and lower ends. Energy deposited by the detonation is trapped between these two interfaces and results in rich wave interactions in the metal layer.

Figure 18 shows the pressure contours of spherical detonation wave penetrating the first copper interface and pushing out the second interface. The first snapshot

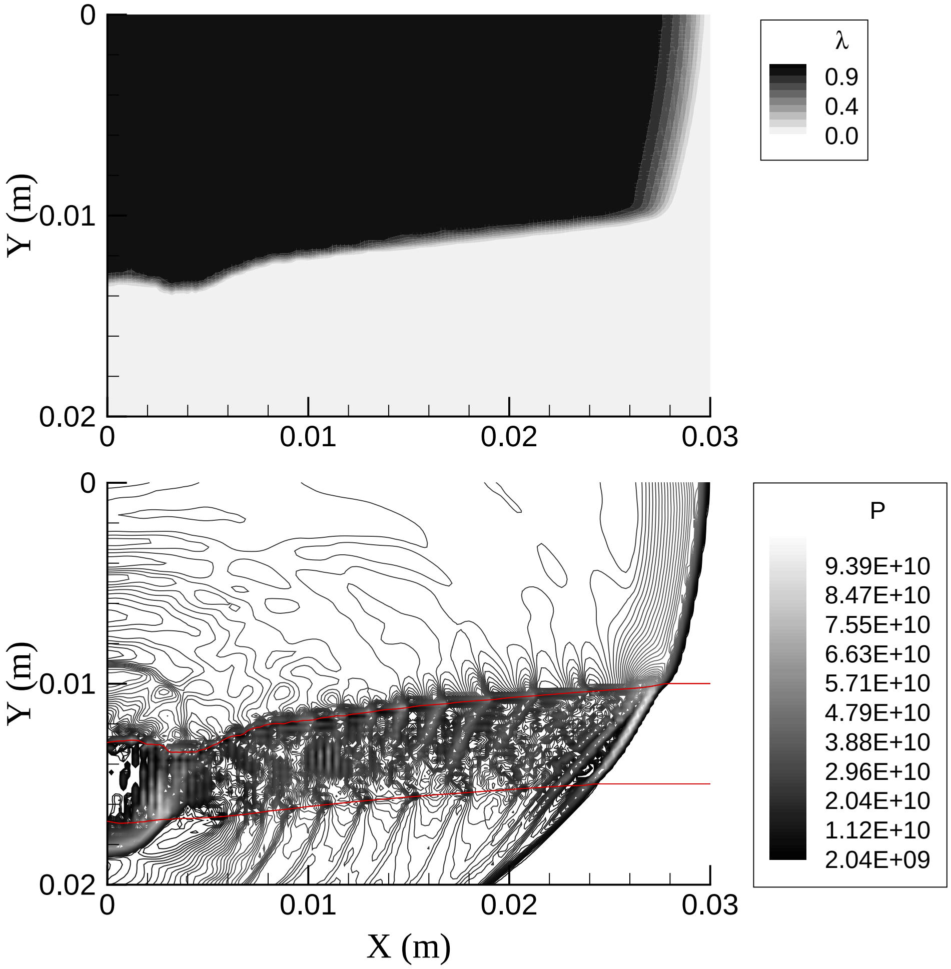

Figure 14. Explosive welding of copper (8.93 g/cc) and high-strength steel (7.85 g/cc). The extent of reaction and the pressure (Pa) are shown. Simulations are carried out on a 150 by 100 grid.

taken at $t = 0.34\,\mu$sec shows a complex wave structure at the interface, where reflections of the incident waves are observed. As the incident spherical wave reaches a second interface, a translational motion of the free boundary is seen at $t = 2.77\,\mu$sec, where part of the incident shock is reflected back toward the first interface. The shock reflections off the upper and lower walls of the domain cause the ends of the plate to bend as shown in the last figure ($t = 5.23\,\mu$sec). This suggests a pinch-off mechanism by which a metal of finite thickness may rupture upon collision with a penetrating

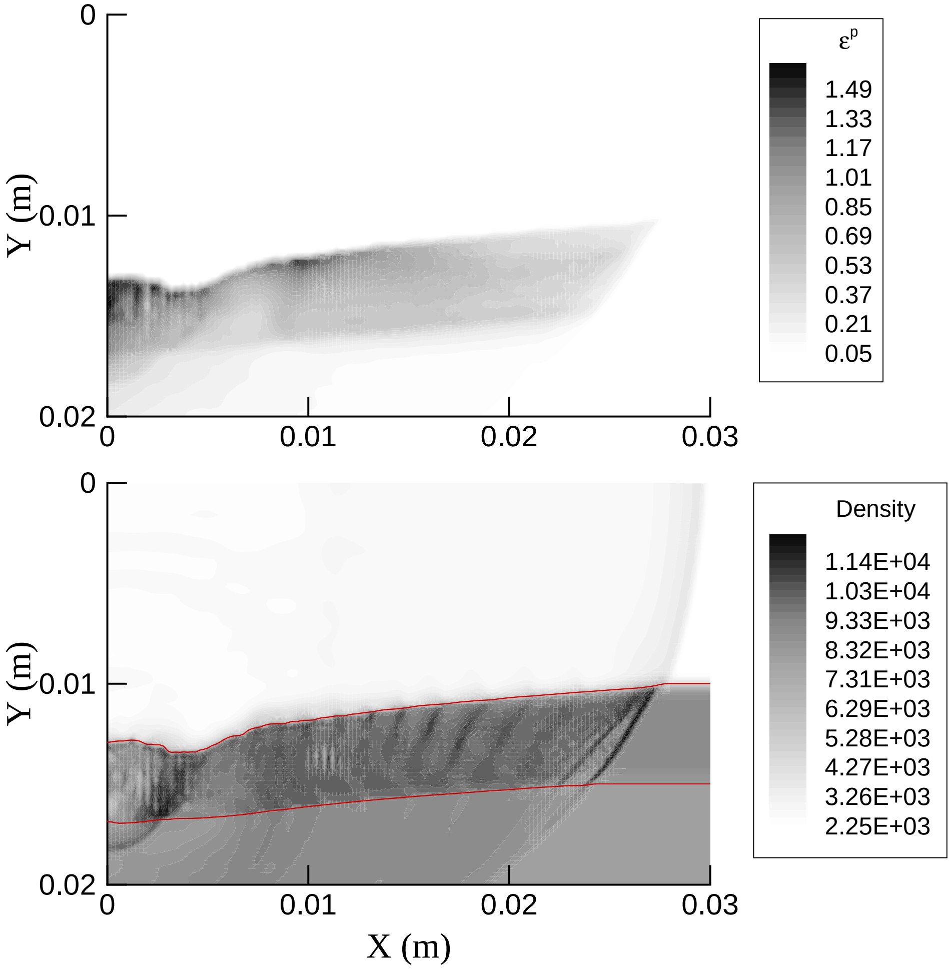

Figure 15. Explosive welding of copper and high-strength steel. Effective plastic strain and the density.

detonation wave. Figure 19 describes how the initially unreacted HE is burnt as the hot product gas pushes the copper plate in the direction outward.

6. Summary and discussion

We have developed a comprehensive numerical framework to compute multi-material interactions for the energetic materials and such other inerts as metal and an elastic solid. The numerical methods used in the spatial discretization are higher-order

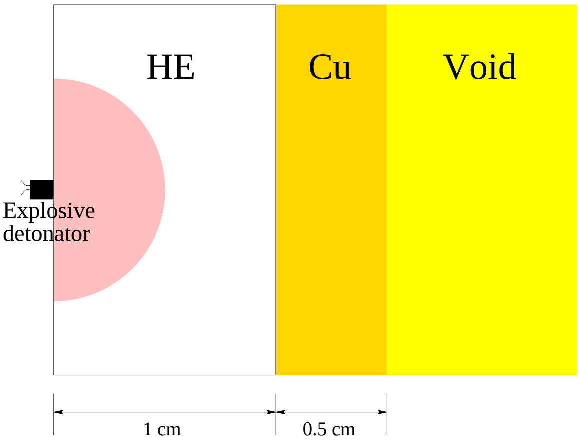

Figure 16. Plate cut experiment. Schematic of copper plate impact by an expanding cylindrical detonation.

ENO schemes with level sets to treat the sharp material interfaces. The level sets track the motions of the material–material or material–void (or vacuum) interfaces so as to minimize any spurious oscillations associated with the smearing of entropy profiles across a sharp material interface. The high-resolution simulation tool for the multi-material impact has been carefully validated through a series of one-dimensional and multi-dimensional tests and has produced both qualitative and quantitative comparisons with benchmark results.

Acknowledgments

This work was carried out with resources from the U. S. Air Force Research Laboratory, Armament Directorate, Eglin AFB, Florida, F08630-00-1-0002 and the U. S. Air Force Office of Scientific Research, Physical Mathematics Directorate, F49620-96-1-0260. The work was performed under the auspices of the U.S. Department of Energy by the University of California, Lawrence Livermore National Laboratory under Contract No. W-7405-Eng-48.

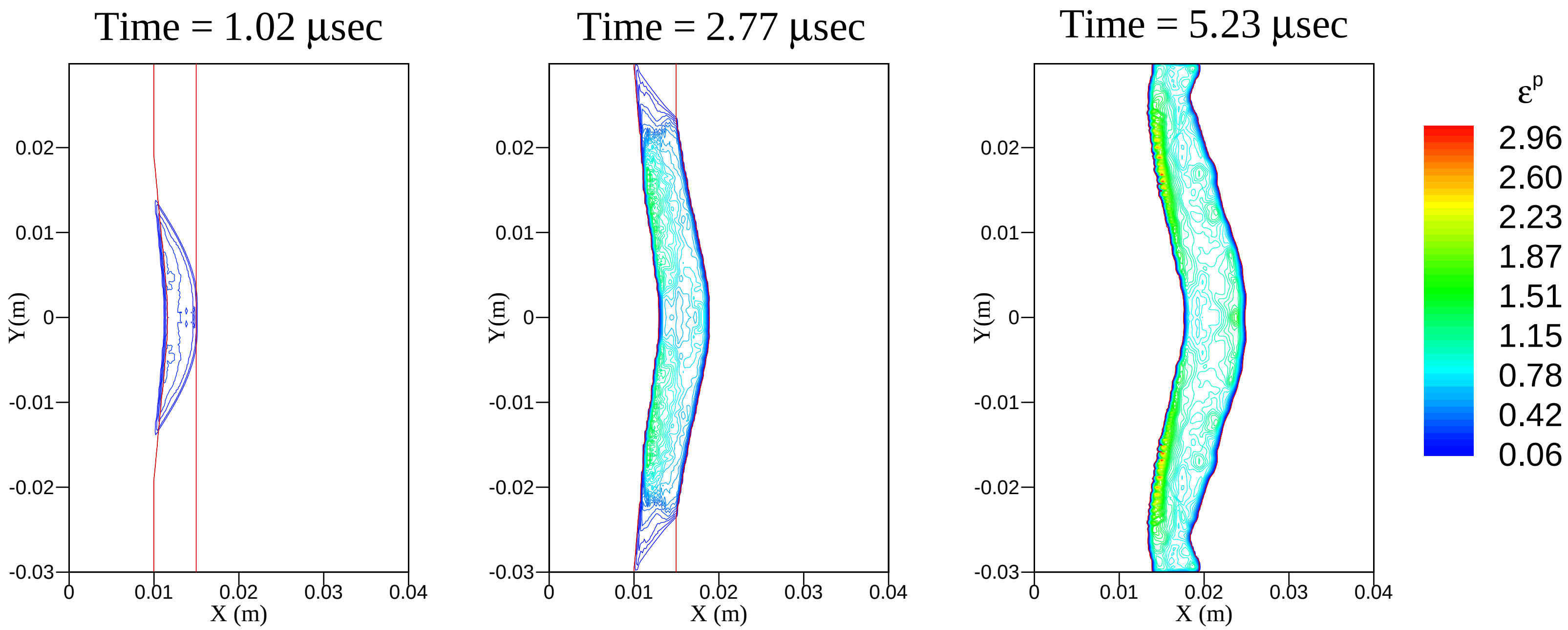

Figure 17. Plate cut experiment. A cylindrical detonation wave is initiated in a cylindrical region centered at $(x, y) = (0, 0)$. The curved detonation strikes copper plate target located at 1 cm. The right edge of the plate is at 1.5 cm, where the copper–void interface boundary is enforced. Dynamic deformation and translation of the plate is illustrated by snapshots at different times. This figure shows the effective plastic strain field simulated on 200 by 600 grid.

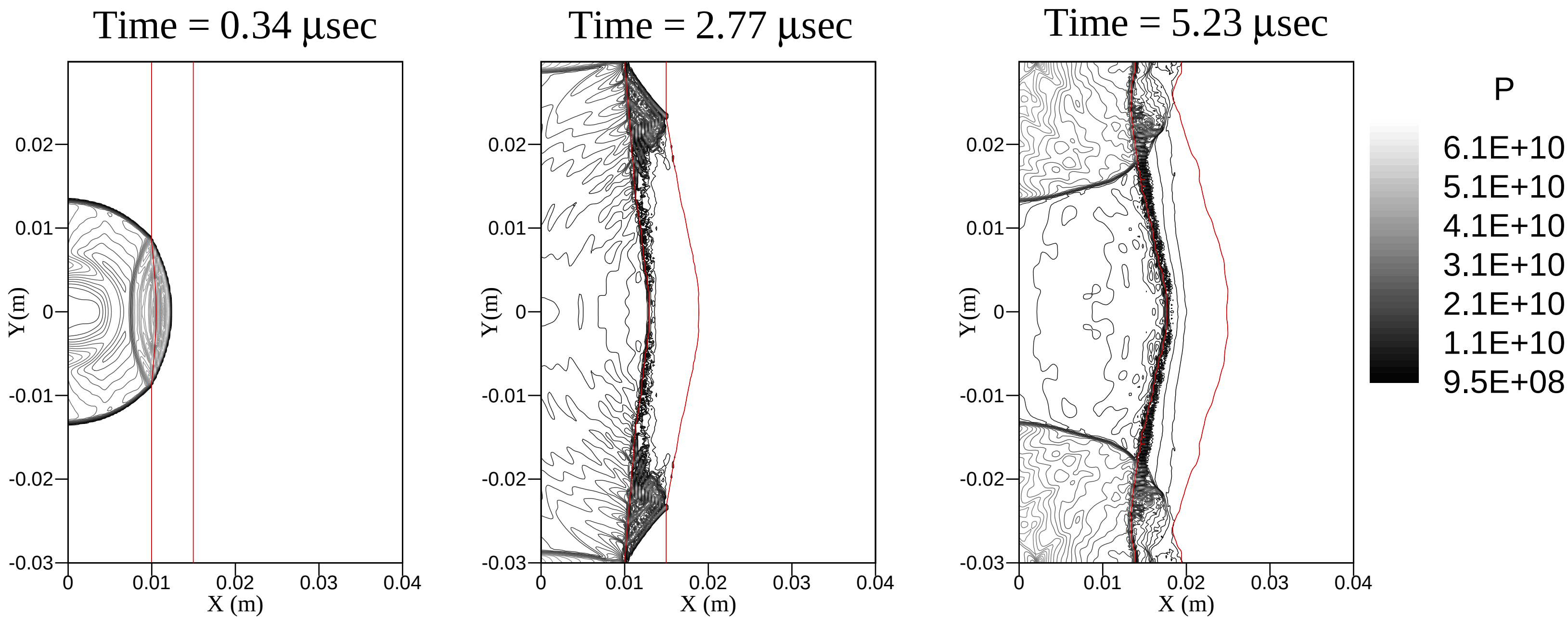

Figure 18. Pressure field for the plate cut experiment shown on 200 by 600 grid.

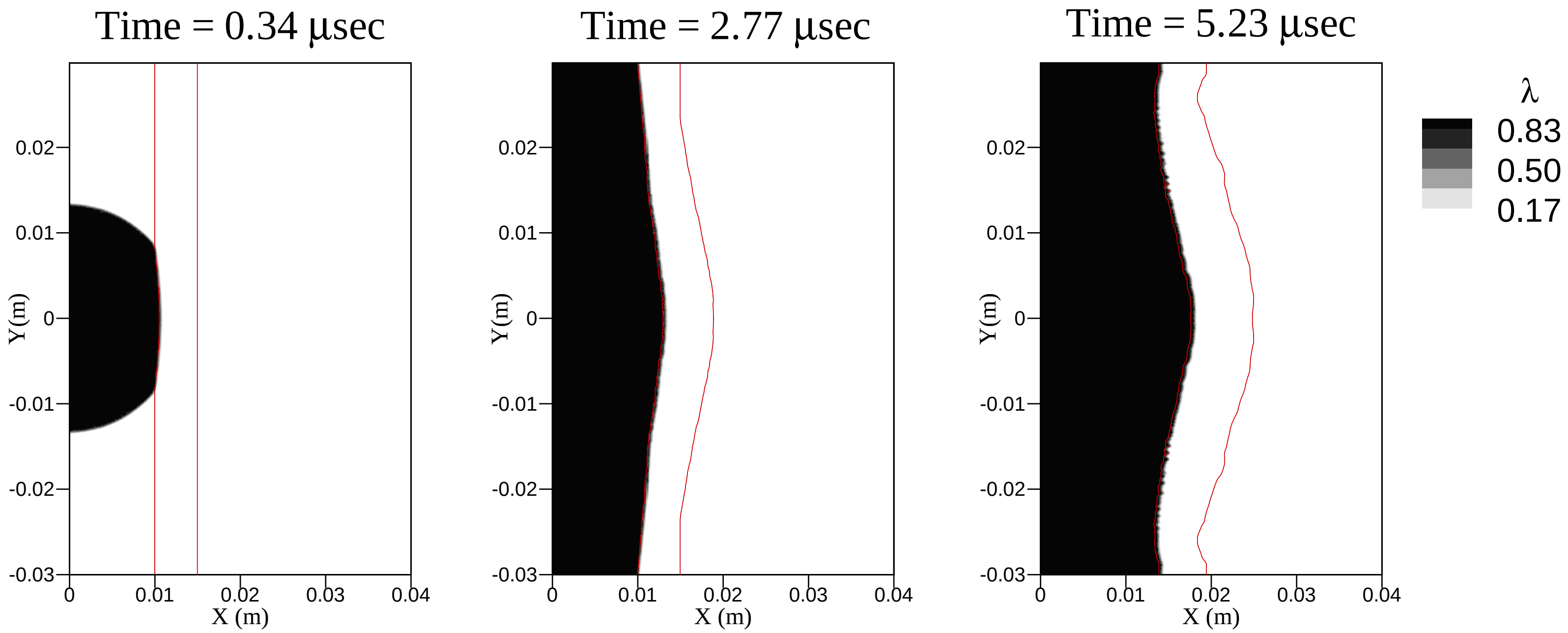

Figure 19. Reaction progress variable for the plate cut experiment shown on 200 by 600 grid.

References

[1] J. M. McGlaun, S. L. Thompson, and M. G. Elrick. CTH: A Three-Dimensional Shock Wave Physics Code. *Int. J. Impact Engineering*, 10:351–360, 1990.

[2] D. B. Kothe, J. R. Baumgardner, et al. PAGOSA: A Massively-Parallel, Multi-Material Hydrodynamics Model for Three-Dimensional High-Speed Flow and High-Rate Material Deformation. *High Performance Computing Symposium*, pages 9–14, 1993.

[3] K. S. Holian and B. L. Holian. Hydrodynamic Simulations of Hypervelocity Impacts. *Int. J. Impact Engineering*, 8:115–132, 1989.

[4] J. M. McGlaun, F. J. Zeigler, and S. L. Thompson. CTH: A Three-Dimensional, Large Deformation, Shock Wave Physics Code. *Shock Waves in Condensed Matter*, pages 717–720, 1987.

[5] T. D. Aslam, J. B. Bdzil, and D. S. Stewart. Level Set Methods Applied to Modeling Detonation Shock Dynamics. *Journal of Computational Physics*, 126:390–409, 1996.

[6] J. J. Yoh. Thermomechanical and Numerical Modeling of Energetic Materials and Multi-material Impact. PhD thesis, Department of Theoretical and Applied Mechanics, University of Illinois at Urbana-Champaign, 2001.

[7] G. T. Camacho and M. Ortiz. Adaptive Lagrangian modelling of ballistic penetration of metallic targets. *Computer Methods in Applied Mechanics and Engineering*, 142:269–301, 1997.

[8] T. D. Aslam and J. B. Bdzil. Private communication. Los Alamos National Laboratory, 2001.

[9] X.-D. Liu and S. Osher. Convex ENO High Order Multi-Dimensional Schemes without Field by Field Decomposition or Staggered Grids. *Journal of Computational Physics*, 142:304–330, 1998.

[10] C.-W. Shu and S. Osher. Efficient Implementation of Essentially Non-oscillatory Schemes II. *Journal of Computational Physics*, 83:32–78, 1989.

[11] C. B. Laney. *Computational Gasdynamics.* Cambridge: Cambridge University Press, 1998.

[12] S. Osher and J. A. Sethian. Fronts Propagating with Curvature-Dependent Speed: Algorithms Based on Hamilton-Jacobi Formulations. *Journal of Computational Physics*, 79:12–49, 1988.

[13] W. Mulder, S. Osher, and J. A. Sethian. Computing Interface Motion in Compressible Gas Dynamics. *Journal of Computational Physics*, 100:209–228, 1992.

[14] R. P. Fedkiw, T. Aslam, B. Merriman, and S. Osher. A Non-Oscillatory Eulerian Approach to Interfaces in Multimaterial Flows (The Ghost Fluid Method). *Journal of Computational Physics*, 152:457–492, 1999.

[15] R. P. Fedkiw, A. Marquina, and B. Merriman. An Isobaric Fix for the Overheating Problem in Multimaterial Compressible Flows. *Journal of Computational Physics*, 148:545–578, 1999.

[16] J. B. Buckmaster and G. S. S. Ludford. *Theory of Laminar Flames.* Cambridge University Press, 1982.

[17] W. Fickett and W. C. Davis. *Detonation.* Berkeley, Calif.: University of California Press, 1979.

[18] D. M. Belk. Class notes. U. S. Air Force Research Laboratory, Eglin Air Force Base, Fla., 1999.

[19] R. F. Davidson and P. J. Maudlin. A continuum code investigation of stress integration using exact and approximate material rotation. Technical Report LA-12380-MS, Los Alamos National Laboratory, NM, 1992.

[20] G. R. Johnson and W. H. Cook. Fracture characteristics of three metals subjected to various strains, strain rates, temperatures and pressures. *Engrg. Fract. Mech.*, 21:31–48, 1985.

[21] S. Xu, T. Aslam, and D. S. Stewart. High Resolution Numerical Simulation of Ideal and Non-ideal Compressible Reacting Flows with Embedded Internal Boundaries. *Combust. Theory*

Modelling, 1:113–142, 1997.

[22] Y. Y. Zhu and S. Cescotto. Unified and mixed formulation of the 4-node quadrilateral elements by assumed strain method: Application to thermomechanical problems. *Int. J. Numer. Methods Engrg.*, 38:685–716, 1995.

[23] R. G. Whirley and J. O. Hallquist. DYNA-3D User Manual. Technical Report UCRL-MA-107254, Lawrence Livermore National Laboratory, 1991.

[24] A. Kamoulakos. A simple benchmark for impact. *Bench Mark*, pages 31–35, 1990.

[25] J. Quirk. A Parallel Adaptive Grid Algorithm for Computational Shock Hydrodynamics. *Appl. Numer. Math.*, 20:427–453, 1996.

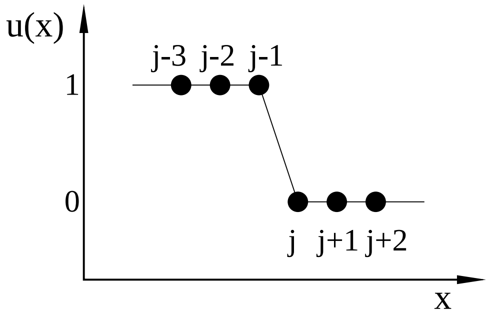

Figure 20. Profile of u on a stencil $(x_{j-3}, x_{j-2}, x_{j-1}, x_j, x_{j+1}, x_{j+2})$ at $t = 0$.

Appendix

We consider a simple 1-D Burger's equation to illustrate the high-order convex-ENO construction.

$$\frac{\partial u}{\partial t} + \frac{\partial f}{\partial x} = 0 \tag{76}$$

where $f = u^2/2$, and the solution at time $t = 0$ is depicted in Fig. 20.

We consider the upwinding procedure using the stencil (x_{j-1}, x_j) and denote $f^+_{j+\frac{1}{2}}$ as the upwind flux. The construction of downwind flux, $f^-_{j+\frac{1}{2}}$, starts with (x_j, x_{j+1}), instead. We first identify that the first and second-order fluxes are the local Lax–Friedrichs fluxes evaluated at x_j. From (5), the first-order ENO flux is

$$f^{(1)+}_{j+\frac{1}{2}}(u_j) = \frac{1}{2}(f(u_j) + \alpha_{j+\frac{1}{2}} u_j). \tag{77}$$

For the second-order upwind flux, we decompose (8) into upwind (+) and downwind (−) components, such that

$$f^{(2)+}_{j+\frac{1}{2}}(u_j) = \frac{1}{2}(f(u_j) + \alpha_{j+\frac{1}{2}} u_j) + \frac{1}{4}(\ell(r^+_j)(\Delta_+ f(u_j) + \alpha_{j+\frac{1}{2}} \Delta_+ u_j)). \tag{78}$$

Up to a second order, general ENO fluxes are identical to convex ENO fluxes that will be described next. For third order, we define a function called primitive function, $H(x)$, such that

$$f(x) = \frac{dH(x)}{dx}. \tag{79}$$

We select three cubic interpolants of H at stencils $(x_{j-3}, x_{j-2}, x_{j-1}, x_j)$, $(x_{j-2}, x_{j-1}, x_j, x_{j+1})$, and $(x_{j-1}, x_j, x_{j+1}, x_{j+2})$, differentiate each of the interpolants, then evaluate the results at x_j, and take the convex combination of these numbers which is "closest" to $\left(H^{(2)+}(x_j)\right)' = f^{(2)+}_{j+\frac{1}{2}}(u_j)$ in (78). The details of the convex ENO construction follow next.

The derivatives of three candidate interpolants are

$$\begin{aligned}\left(H_1^{(3)+}(x_j)\right)' &= (f[x_{j-2},1] + \alpha_{j+\frac{1}{2}}u[x_{j-2},1]) + (f[x_{j-1},2] + \alpha_{j+\frac{1}{2}}u[x_{j-1},2])(5\Delta x)\\ &\quad +(f[x_j,3] + \alpha_{j+\frac{1}{2}}u[x_j,3])(11(\Delta x)^2), \qquad (80)\\ \left(H_2^{(3)+}(x_j)\right)' &= (f[x_{j-1},1] + \alpha_{j+\frac{1}{2}}u[x_{j-1},1]) + (f[x_j,2] + \alpha_{j+\frac{1}{2}}u[x_j,2])(3\Delta x)\\ &\quad +(f[x_{j+1},3] + \alpha_{j+\frac{1}{2}}u[x_{j+1},3])(2(\Delta x)^2), \qquad (81)\\ \left(H_3^{(3)+}(x_j)\right)' &= (f[x_j,1] + \alpha_{j+\frac{1}{2}}u[x_j,1]) + (f[x_{j+1},2] + \alpha_{j+\frac{1}{2}}u[x_{j+1},2])(\Delta x)\\ &\quad +(f[x_{j+2},3] + \alpha_{j+\frac{1}{2}}u[x_{j+2},3])(-(\Delta x)^2), \qquad (82)\end{aligned}$$

where one of these three candidates (ν_o) becomes the upwind flux at x_j (i.e. $f^{(3)+}_{j+\frac{1}{2}} = \left(H_{\nu_o}^{(3)+}(x_j)\right)'$). Evaluating the convex-weighted differences as in (24), we can decide on the interpolant whose absolute value of the difference is the minimum.

Table 8 summarizes the calculated upwind fluxes at x_j based on the convex ENO construction for the given example problem.

Since the first and second-order fluxes are the general ENO fluxes using minmod limiter, we will just use $f^{(1)+}_{j+\frac{1}{2}}(u_j)$ and $f^{(2)+}_{j+\frac{1}{2}}(u_j)$ to build the third-order convex ENO flux, $f^{(3)+}_{j+\frac{1}{2}}(u_j)$. To do this, we first evaluate the divided differences of u and f following the definitions in (13), such that

$$u[x_{j-2},1] = 0, \quad u[x_{j-1},1] = \frac{1}{\Delta x}, \quad u[x_j,1] = -\frac{1}{\Delta x}, \quad u[x_{j+1},1] = 0, \quad u[x_{j+2},1] = 0,$$

Table 8. Summary of convex-ENO fluxes evaluated at x_j.

x	u	$f = u^2/2$	$\alpha_{j+\frac{1}{2}}$	$\ell(r_j^+)$	$f_{j+\frac{1}{2}}^{+(1)}(u_j)$	$f_{j+\frac{1}{2}}^{+(2)}(u_j)$	$f_{j+\frac{1}{2}}^{+(3)}(u_j)$
x_{j-3}	1	$\frac{1}{2}$	1	1			
x_{j-2}	1	$\frac{1}{2}$	1	1			
x_{j-1}	1	$\frac{1}{2}$	1	0			
x_j	0	0	0	1	0	0	$-\frac{1}{6\Delta x}$
x_{j+1}	0	0	0	1			
x_{j+2}	0	0	0	1			

$$u[x_{j-1},2] = \frac{1}{2(\Delta x)^2}, \quad u[x_j,2] = -\frac{1}{(\Delta x)^2}, \quad u[x_{j+1},2] = \frac{1}{2(\Delta x)^2}, \quad u[x_{j+2},2] = 0,$$
$$u[x_j,3] = -\frac{1}{2(\Delta x)^3}, \quad u[x_{j+1},3] = \frac{1}{2(\Delta x)^3}, \quad u[x_{j+2},3] = -\frac{1}{6(\Delta x)^3}$$

and

$$f[x_{j-2},1] = 0, \quad f[x_{j-1},1] = 0, \quad f[x_j,1] = -\frac{1}{2\Delta x}, \quad f[x_{j+1},1] = 0, \quad f[x_{j+2},1] = 0,$$
$$f[x_{j-1},2] = 0, \quad f[x_j,2] = -\frac{1}{4(\Delta x)^2}, \quad f[x_{j+1},2] = \frac{1}{4(\Delta x)^2}, \quad f[x_{j+2},2] = 0,$$
$$f[x_j,3] = -\frac{1}{12(\Delta x)^3}, \quad f[x_{j+1},3] = \frac{1}{6(\Delta x)^3}, \quad f[x_{j+2},3] = -\frac{1}{12(\Delta x)^3}.$$

Evaluating the three candidate fluxes in (80) through (82), we find

$$\left(H_1^{(3)+}(x_j)\right)' = -\frac{11}{12\Delta x}, \quad \left(H_2^{(3)+}(x_j)\right)' = -\frac{5}{12\Delta x}, \quad \left(H_3^{(3)+}(x_j)\right)' = -\frac{1}{6\Delta x}.$$

Now, we apply the convex ENO decision by evaluating the differences,

$$d_1 = -c_1 \frac{11}{12\Delta x}, \quad d_2 = -c_2 \frac{5}{12\Delta x}, \quad d_3 = -c_3 \frac{1}{6\Delta x},$$

with positive definite coefficients, c_1, c_2, and c_3, defined previously. Since all three differences are of the same sign, we identify d_3 as having the absolute minimum value, and find

$$f_{j+\frac{1}{2}}^{(3)+}(u_j) = \left(H_3^{(3)+}(x_j)\right)' = -\frac{1}{6\Delta x}.$$

The third-order local Lax–Friedrichs flux is thus constructed by adding up the upwind (+) portion as shown above and the downwind portion analogously evaluated at (x_j, x_{j+1}):

$$\hat{f}_{j+\frac{1}{2}} = f^{(3)+}_{j+\frac{1}{2}}(u_j) + f^{(3)-}_{j+\frac{1}{2}}(u_{j+1}) = \left(H^{(3)+}(x_j)\right)' + \left(H^{(3)-}(x_{j+1})\right)'. \qquad (83)$$